Acta Astronautica 246 (2026) 201–214

Contents lists available at ScienceDirect

Acta Astronautica

journal homepage: www.elsevier.com/locate/actaastro

Processing and optical properties of Martian regolith for solar energy applications

Mariano Casu [a], Roberto Orrù [a,b], Roberta Licheri [a,b], Alessandro Concas [a,b], Giacomo Cao [a,b], Costantino Cau [c], Sebastiano Garroni [c], Aldo Dell'Oro [d,e], Elisa Sani [e,d,*]

[a] Dipartimento di Ingegneria Meccanica, Chimica e dei Materiali, Unità di Ricerca del Consorzio Interuniversitario Nazionale per la Scienza e Tecnologia dei Materiali (INSTM), Università degli Studi di Cagliari, via Marengo 2, 09123, Cagliari, Italy
[b] Interdepartmental Centre of Environmental Science and Engineering (CINSA), University of Cagliari, Via San Giorgio 12, 09124, Cagliari, Italy
[c] Dipartimento di Scienze Chimiche, Fisiche, Matematiche e Naturali, Università degli Studi di Sassari, 07100, Sassari, Italy
[d] Istituto Nazionale di Astrofisica (INAF), Osservatorio Astrofisico di Arcetri, Largo E. Fermi, 5, I-50125, Firenze, Italy
[e] CNR-INO Istituto Nazionale di Ottica, Largo E. Fermi, 6, I-50125, Firenze, Italy

ARTICLE INFO

Keywords:
Space resources
ISRU
Martian regolith simulants
SPS
Optical properties
Solar absorber

ABSTRACT

In-situ exploitation of Martian resources to obtain products and services is crucial for promoting future manned missions on the planet. Along this line, the JSC-Mars-1A, and MMS regolith simulants which are representative of the wide spectrum of soils available on the Mars surface, are investigated in detail to evaluate their possible utilization for solar energy applications, when used either in powder form or after being consolidated by Spark Plasma Sintering (SPS). The markedly different densification behavior shown by the two simulants can be associated with their diverse compositional and structural characteristics, with the predominant amorphous constituent (about 50 wt%) in original JSC-Mars-1A observed to strongly favor powder consolidation. For this system, fully dense samples were obtained by SPS at 1000 °C/3min/30 MPa. Concurrently, the amorphous fraction was reduced to 16 wt%. In contrast, the highly crystalline nature of MMS (70 wt% of Andesine, only 3 wt % of the amorphous content) makes this simulant more thermally stable and less prone to be consolidated, with 97.5% dense samples produced by SPS at 1050 °C/3min/30 MPa.

To assess the samples' solar absorption and thermal radiation properties, optical spectra of both simulants in the range from 0.2 to 16 μm wavelength were compared by considering pristine powders and bulk samples with different porosity and roughness characteristics. We found a significantly increased solar absorptance in the sintered samples with respect to the starting powders, even reaching the remarkable value of 0.93. The thermal emittance of ceramics was lower than that of powders for temperatures below about 300K, and superior for higher temperatures. These results have been discussed regarding the possible application of solar energy harvesting and thermal energy storage.

1. Introduction

In the last decades, research and development of new technologies and solutions for the exploration and colonization of nearby extraterrestrial bodies saw an increase in the involved players, which nowadays include not only space agencies of the major superpowers but also emerging space programs both from new geopolitical agents and private investors [1,2].

In this context, the Moon is widely regarded as a strategic staging ground for deep-space missions, while Mars represents the primary long-term objective for human exploration and potential settlement [3–7].

Earth-based space exploration is associated with high costs, as all mass launched to Low Earth Orbit (LEO) and beyond needs to escape the planet's gravitational field relying on the power generated by the rocket's propellant. On this basis, the development of *In-Situ* Resource Utilization (ISRU) technologies and techniques, whose purpose is to harness and utilize space resources to obtain products and services which significantly reduce the mass, cost and risk of near- and long-term space exploration, allows payload costs associated with longer-term missions to be cut [8]. This approach is particularly relevant for Mars, given its distance from Earth, relatively strong gravitational field, and locally available resources. Current mission architectures estimate a

* Corresponding author. CNR-INO Istituto Nazionale di Ottica, Largo E. Fermi, 6, I-50125, Firenze, Italy.
E-mail address: elisa.sani@ino.cnr.it (E. Sani).

https://doi.org/10.1016/j.actaastro.2026.03.043
Received 24 April 2025; Received in revised form 23 February 2026; Accepted 22 March 2026
Available online 1 April 2026

minimum duration of approximately 500 days for short-stay missions [9,10], emphasizing the need for a high autonomy in future permanent bases.

Among the ISRU strategies to be developed, *in-situ* surface power generation and storage represents one of the key aspects identified by NASA, along with the utilization of locally available resources for a broad range of scopes [8].

In this context, the most abundant and ubiquitous material available on the Martian surface is certainly represented by regolith [11]. It typically shows a globally homogeneous basaltic nature with local to regional enrichments in secondary minerals, reflecting specific geological histories. Given the complexity and energy requirements for the separation of different mineral phases, single metals or other elements, the direct utilization of regolith is then considered preferable. Differently from Lunar soil, Martian regolith has not been yet brought to Earth, so that all the research work performed to date on this subject makes use of regolith analogues [11,12]. In this framework, JSC-Mars-1A and Mojave Mars Simulant (MMS) are two of the most investigated Martian regolith simulants developed so far [11].

As for their possible exploitation for energy generation and storage, while several works assessed the feasibility of the use of untreated or sintered Lunar regolith as solar energy absorbers [13] and thermal energy storage (TES) materials [14–17], to date, to the best of our knowledge, no systematic investigation has been reported on Martian regolith simulants that links processing techniques—such as Spark Plasma Sintering—with the resulting microstructural, densification, and optical properties relevant for those applications on the Martian surface.

Generally, sintered regolith is considered the best option for TES, given the enhanced thermal conductivity and mechanical properties of bulk materials if compared to loose dust [14,18].

Accordingly, different consolidation methods, previously applied to terrestrial processes, have been considered to convert loose Martian regolith into sintered bodies. They include pressureless sintering [19], combustion synthesis-based processes [20–22], impact compaction [23], high-pressure consolidation [23], solar sintering [24], additive manufacturing [25,26], and cold sintering [27]. For solar-thermal applications, optical properties are critical. They are different, and process-dependent, for powders and their sintered bulks [13].

Spark Plasma Sintering (SPS), also referred to as Electric Current-Assisted Sintering (ECAS), is a widely used efficient consolidation method able to guarantee the achievement of high densification levels in very short times, compared to standard hot pressing or pressureless sintering [28]. Recently, the SPS technology has been successfully applied to process lunar regolith simulants [13,29–32].

The low energy demand associated with this technique is expected to be highly beneficial for its applicability in contexts such as the proposed Martian outposts. Moreover, the operating conditions typical of the SPS setup, which requires high vacuum during experimental runs, simulate, more closely, the actual Martian atmosphere compared to air sintering. Furthermore, this technique also allows for the obtainment of adequate densification levels without employing additional binders, which may not be available in-situ.

In the present work, the JSC-Mars-1A and MMS simulants are first characterized in terms of mineralogy, thermal stability, and density. Despite their widespread use, complete datasets—including theoretical densities and other key parameters—remain scarce [11].

The simulants are consolidated via SPS at different temperatures and mechanical loads to produce bulk specimens, whose composition, density, porosity, and surface roughness are evaluated. Finally, spectral absorptance/emittance, as well as integrated solar absorptance and thermal emittance are studied in the temperature range of 100-600 K, representative of potential ISRU-based Martian operating conditions. In the latter regard, it should be further emphasized that, in contrast with lunar regolith, whose optical and thermal radiative properties have been recently evaluated for solar energy applications [13], no previous studies are available so far in literature on Martian regolith simulants addressing energy-related functional properties to target the use of regolith for solar thermal energy generation and storage on Mars.

2. Experimental materials and methods

2.1. Regolith simulant powders

The Johnson Space Center Martian regolith simulant (JSC-Mars-1A, <1 mm class, Orbital Technologies Corporation, Madison, WI, USA) used in this work consists of a red/brown volcanic ash mined from a cinder quarry in the Pu'u Nene crater of the Mauna Kea volcano (near Hilo, Hawaii, USA) sieved to the <1 mm fraction [33]. On the other hand, the MMS simulant, provided by the Jet Propulsion Laboratory (Pasadena, USA), is a gray/brown basalt mined from the Saddleback Mountain in the Mojave Desert (near Boron, California, USA) [34].

The chemical compositions (oxide constituents, wt.%) of the two simulants are reported in Table 1, along with data relative to actual Martian soil obtained in the framework of Viking 2, Pathfinder and MER Opportunity missions [35–37].

Thermo-gravimetric analyses were performed on pristine JSC-Mars-1A and MMS using a simultaneous DTA-TGA Instrument (NETZSCH STA 409 PC Luxx, Germany). The tests were designed with a heating rate of 2 K/min from room temperature (RT) to 800 °C.

Prior to SPS experiments, JSC Mars-1A powders were first heat treated in air at 700 °C for 2 h using a muffle furnace (LT 24/11/B410, Nabertherm, Lilienthal, Germany), and then stabilized in air environment at RT.

Absolute densities of the two materials were determined by a gas displacement pycnometer (AccuPyC 1340, Micromeritics, USA) using helium as adsorbate gas.

The pristine JSC Mars-1A simulant received a 60 min ball milling treatment (balls to powder weight ratio equal to 2) using a planetary mill (Tecnotest, Italy) to reduce the original powders size (<1 mm) to less than 150 μm. Such treatment was not needed in the case of MMS, which already satisfied the latter condition. Particle size distribution of both powder batches was evaluated by a laser light scattering analyzer (CILAS 1180, France).

2.2. Sintered samples

Regolith powders were consolidated by SPS (515S model, Fuji Electronic Industrial Co., Ltd., Kanagawa, Japan) under vacuum conditions (about 20 Pa). Approximately 2.15 g of either pristine (MMS) or heat treated (JSC-Mars-1A) simulants were located inside a die cylinder (30.2 mm external diameter, 20.7 mm inside diameter, 48 mm height)

Table 1
Oxide constituents (wt%) of JSC Mars-1A and MMS simulants. Data for actual Martian soil from Viking 2 landing site, Pathfinder and MER Opportunity are also reported for comparison. (n.r.: not reported).

Oxide	JSC Mars-1A [38]	MMS [34]	Viking Lander 2 [35]	Pathfinder soil [36]	MER Opportunity soil [37]
SiO_2	34.5 - 44	49.4	43	42	43.8
Al_2O_3	18.5 - 23.5	17.10	7	10.3	8.6
Fe_2O_3	9 - 12	10.87	17.8	21.7	n.r.
CaO	5 - 6	10.45	5.7	6.1	6.67
TiO_2	3 - 4	1.09	0.56	0.8	1.08
FeO	2.5 - 3.5	n.r.	n.r.	14.2	15.6
MgO	2.5 - 3.5	6.08	6	7.3	7.1
Na_2O	2 - 2.5	3.28	n.r.	2.8	1.6
P_2O_5	0.7 - 0.9	0.17	n.r.	0.7	0.83
K_2O	0.5 - 0.6	0.48	<0.15	0.6	0.44
MnO	0.2 - 0.3	0.17	n.r.	0.3	0.36
Cr_2O_3	n.r.	0.05	n.r.	0.3	0.46
SO_3	n.r.	0.10	8.1	6.0	5.57
LOI	n.r.	(3.39)	n.r.	n.r.	n.r.

equipped with two plungers (20 mm diameter, 34 mm height), all consisting of AT101 graphite (ATAL Srl., Italy). A graphite foil (0.13 mm thickness, Alfa Aesar, Karlsruhe, Germany) was placed in between the sample and the inner walls of die/plungers to make sample release easier after SPS. During sintering experiments, temperature was measured by a K-type thermocouple (TC Misure e Controlli S.R.L., Italy) inserted in a small hole drilled on the external die surface. The use of a 3 mm thick graphite felt (Atal s.r.l., Italy) covering the die was aimed to limit heat losses during the sintering process. Each sample was first cold compacted in the SPS apparatus at 15 MPa for about 10 min. Then, the electric current was applied to heat powders first from the RT to an intermediate level, 100 °C below the maximum value (T_D), at a rate of 50 °C/min. Then, to reduce possible overshooting problems, the heating rate was lowered (10 °C/min) until the T_D value was achieved. The sample was maintained for 3 min at T_D and, finally, the temperature was decreased following a prescribed cooling program. The influence of the temperature on samples density was investigated in the ranges 800-1000 °C and 950-1050 °C for the cases of JSC-Mars-1A and MMS systems, respectively. The effect produced by an increase of the applied mechanical pressure (P) from 15 to 30 MPa was also explored.

While the displacement output recorded in real time provides an indication of the evolution of the sample densification during SPS, the thermal expansion of graphite tools, electrodes and the sample is also responsible for the measured value. The latter contribution, but that of the sample, was evaluated separately under the same SPS conditions. The so-called sample shrinkage (δ), a more reliable index of the densification degree, was then determined.

The obtained bulk samples (about 20 mm diameter and 1.8 to 3 mm height) were properly polished using abrasive paper, to remove possible residual impurities from the graphite tools. Each experimental condition was replicated at least twice.

Samples density was measured by the Archimedes' method using acetone as soaking medium (as suggested by the work of Sizemore and Mellon [39]) and an analytical balance (±0.0005 g precision) (Ohaus Explorer Pro, Ohaus Corporation, NJ, USA) to weigh them. Relative densities were then evaluated by considering, as reference values, the absolute densities of original JSC-Mars-1A and MMS simulants, as described previously.

To verify the capability of the sintered samples to withstand temperature changes occurring on Mars during the course of each sol [40], they were subjected to thermal cycles. The latter ones consisted in exposing JSC-Mars-1A and MMS samples for 12 h at −80 °C (~193K) (ACS Polar 550H, Angelantoni, Italy) followed by 12 h at RT. After the test, samples were also examined by a Keyence VHX-S770E digital microscope (KEYENCE ITALIA S.p.A., Italy) to verify that no cracks were formed.

X-Ray Powder Diffraction of the simulants, (pristine, heat treated and sintered) were carried out in a Rigaku SmartLab (Bragg-Brentano geometry) equipped with a rotating copper anode (Cu Kα radiation λ = 1.5418 nm) working at 40 kV and 100 mA. The analysis was performed, in the 5°-130° theta/2theta range, with a step-size of 0.05° and for 30 s for each step. The attribution of the mineralogical phases was performed with QualX [41], with a Search and Match approach, using the COD (Crystallography Open Database) as a reference database [42]. Crystallographic studies in terms of relative abundance, crystallite size, crystal disorder, and cell parameters were estimated by the Rietveld method, using MAUD (Material Analysis Using Diffraction) program [43]. The CIF files used for the Rietveld refinement were provided by the COD Database [42].

The microstructural characteristics of the samples surface were examined by SEM (Zeiss Evo LS 15).

Surface roughness of the polished samples selected for optical measurements was determined using a contact profilometer (Mitutoyo SJ-201). In particular, the following roughness parameters were considered: Ra, defined as the arithmetic mean of the absolute ordinate Z(x) referring to the length of the measurement profile; Rq defined as the root mean square error for the absolute ordinate Z(x); Rz, influenced by the surface defects, representing the sum of the maximum height of a peak and the maximum depth of a valley (maximum height of the profile along z).

To estimate surface porosity of the sintered samples, SEM micrographs were analyzed using the open-source software GNU Image manipulation Program GIMP (version 2.10). In particular, SEM images were further processed, i.e. brightness and contrast correction, to better evidence pores. Porosity was determined as the ratio of pixels ascribed to pores to total pixels.

Thermal conductivity at RT of sintered samples was estimated following the **Brigaud and Vasseur (1989)** approach [44]. Accordingly, a rule of mixture, based on mineralogical composition and thermal conductivity data of each constituent, taken from **Horai and Simmons (1969)** [45], was used. Values for fully dense materials (k_s) were first determined. Porosity degree (γ) was then considered to evaluate sample conductivity (k) using Loeb's equation [46]:

$$k = k_s(1-\gamma) \tag{1}$$

or Landauer's relation [46]:

$$k = \frac{1}{4}\left\{k_p(3\gamma-1)+k_s(2-3\gamma)+\left\{\left[k_p(3\gamma-1)+k_s(2-3\gamma)\right]^2+8k_sk_p\right\}^{\frac{1}{2}}\right\} \tag{2}$$

when γ <15% or 15%<γ<65%, respectively. Pores conductivity (k_p) was neglected in this work due to the rarefied Martian atmospheric conditions [47].

2.3. Optical properties

Optical properties of both sintered samples and pristine powders were investigated in order to evaluate how they behave when subjected to electromagnetic radiation of different nature. Spectral hemispherical optical reflectance and transmittance were measured in the range 0.19-16.00 μm wavelength using two instruments: a double-beam spectrophotometer (Perkin Elmer Lambda900) with a 150-mm diameter Spectralon®-coated integrating sphere for the spectral range 0.19-2.50 μm, and a Fourier Transform spectrophotometer (Thermo Fisher iS50) with a gold-coated integrating sphere and a liquid N_2-cooled detector for the wavelength region from 2.5 to 16.0 μm. The transmittance and reflectance data have been taken for normal or quasi-normal light incidence angle, respectively.

As a preliminary step, we measured the hemispherical transmittance t∩(λ), finding it to be zero across the whole spectral range investigated, within the experimental uncertainty. Therefore, the normal spectral absorptance α(λ) can be obtained from the experimentally acquired normal hemispherical reflectance r'∩(λ) according to the following relation:

$$\alpha(\lambda) = 1 - t\cap(\lambda) - r'\cap(\lambda) = 1 - r'\cap(\lambda) \tag{3}$$

Being the surfaces at thermal equilibrium, Kirchhoff's law of absorptance applies [48]. Therefore, the normal spectral absorptance α(λ) is equal to the normal spectral emittance ε(λ):

$$\alpha(\lambda) = \varepsilon(\lambda) \tag{4}$$

Then, the total solar absorptance in the wavelength range (λ_{min}, λ_{MAX}) can be obtained by spectral integration as:

$$\alpha = \frac{\int_{\lambda\ min}^{\lambda\ MAX}\alpha(\lambda)\cdot I_{Sun}(\lambda)\cdot d\lambda}{\int_{\lambda\ min}^{\lambda\ MAX} I_{Sun}(\lambda)\cdot d\lambda} \tag{5}$$

And, similarly, the total thermal emittance at temperature T as:

$$\varepsilon(T) = \frac{\int_{\lambda\ min}^{\lambda\ MAX}\varepsilon(\lambda)\cdot I_{BB,T}(\lambda)\cdot d\lambda}{\int_{\lambda\ min}^{\lambda\ MAX} I_{BB,T}(\lambda)\cdot d\lambda} \tag{6}$$

where the integration boundaries λ_{min} = 0.19 μm, λ_{MAX} = 16.0 μm, correspond to the boundaries of the spectral range experimentally accessible in our case, $I_{Sun}(\lambda)$ is the solar irradiance as described below, and $I_{BB,T}(\lambda)$ is the blackbody irradiance at the temperature T:

$$I_{BB,T} = \frac{2\pi hc^2}{\lambda^5} \frac{1}{e^{\frac{hc}{\lambda kT}} - 1} \quad (7)$$

with h, c and k the Planck's constant, the speed of light and the Boltzmann's constant, respectively. As discussed elsewhere [49], the values of α and ε(T) obtained from room-temperature spectra, which are widely used in the literature to characterize solar energy materials, should be considered as approximate values. They cannot represent the values in operative conditions, which would need the knowledge of the spectra at the considered temperatures. They are, however, very useful for a first comparison among a set of samples, as well as to allow the comparison with materials already investigated in the literature. For this reason, this work will consider two significant decimal digits for α and ε(T) calculated from Eqs. (5) and (6), despite the actual propagated uncertainty from the experimental uncertainties on the reflectance and transmittance measurements (±2 on the absolute measured values, which are normalized to 100) would be lower.

Unlike the Lunar case, where the absence of any atmosphere allows to consider the extraterrestrial solar irradiance [50] as representative of the solar irradiance on the surface of the celestial body [13], for Mars planet the actual solar irradiance on the surface must be considered. It is site- and season-dependent, due to the characteristics of Mars atmosphere and orbit.

For the sake of clarity, a schematic picture summarizing the workflow, from the starting powders to the various characterizations, is shown in Fig. 1.

3. Results and discussion

3.1. Characterization of initial simulants

The TGA curves reported in Fig. 2 evidence the different behavior manifested by the two pristine simulants when they are exposed to progressively higher temperatures, up to 800 °C. JSC-Mars-1A clearly shows a superior weight loss (about 28%) compared to MMS (about 8%). These results are fairly consistent with **Chow et al.** [33] and **Corrias et al.** [20] findings relative to JSC-Mars-1A (about 30%) and MMS (about 5%), respectively.

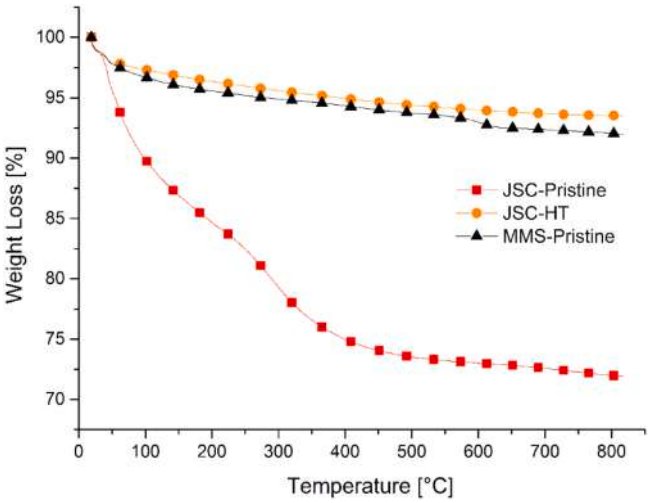

Fig. 2. Weight change (%) of JSC-Mars-1A (before and after the heat treatment carried out for 2h at 700 °C) and MMS simulants during TGA experiment under dynamic conditions.

As seen in Supplementary Fig. S1, and reported by **Karl et al.** [11], some plant roots are found in the JSC-Mars-1A original material. This provides direct evidence of the presence of an organic source. This is also confirmed by the significant carbon content, in the range 3.01-3.16 wt% [23,51], as well as by the traces of ammonium nitrates [51] detected on this simulant. Even if the presence of organics (in traces) on Mars cannot be excluded [52], the large amount found in JSC-Mars-1A needs to be significantly reduced to closely mimic the actual Martian soil characteristics.

Nonetheless, the marked mass loss observed during TGA test of JSC-Mars-1A should be mostly attributed to the presence of water. Based on measurements of the Curiosity rover in the Gale crater [53] the observed water release is far greater than that expected on Martian soil [11,54]. To remove excess water and organic species, JSC-Mars-1A was, before being further processed, heat treated for 2h at 700 °C, above which the related TGA curve does not indicate further weight changes (Fig. 1). As shown in Supplementary Fig. S2**, heat treated powders regained some**

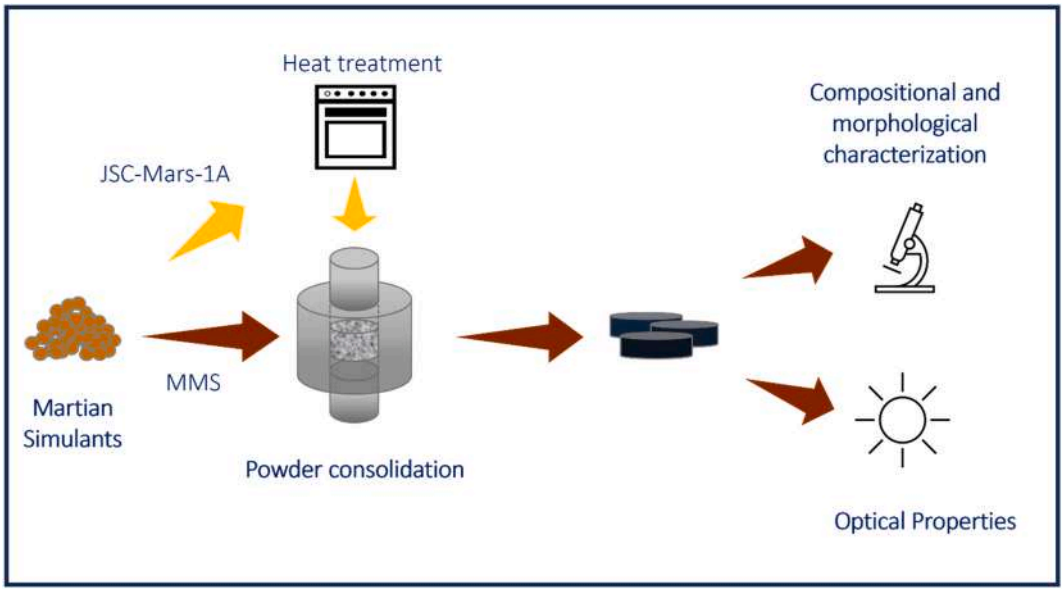

Fig. 1. Schematic representation of the workflow, showing the different processing and characterization steps.

weight when exposed to air environment. This phenomenon, ascribed to the high hygroscopicity of JSC-Mars-1A [34], **can be considered roughly completed within 3 days** (Supplementary Fig. S2).

Fig. 2 also evidenced that the TGA curve associated with the latter material is nearly close to that of untreated MMS, with a measured mass loss of the first simulant equal to about 7 wt%. The characteristics of both pristine MMS and treated JSC-Mars-1A appear now to be more coherent with Martian mission's findings regarding the limited water content in regolith.

To homogenize the coarser JSC-Mars-1A simulant (<1 mm particle size), the related powders were mildly ball-milled to obtain particles smaller than 150 μm. In contrast, pristine MMS did not need any milling step. Particle size parameters of the two simulants are reported in Table 2.

Mineralogic composition of as received simulants and heat treated JSC-Mars-1A was deduced by XRD analysis. The related patterns are reported in Fig. 3. After the identification of the mineral components, their relative content (wt.%) was evaluated, together with crystallographic parameters, with the Rietveld method. The obtained results are shown in Table 3. Each of the simulants presents a relevant texture effect due to the oriented crystal growth typically observed in natural minerals. The corresponding crystallite size, microstrain, and lattice parameters, also estimated with the Rietveld method, are reported in Supplementary Table S1–S4.

XRD of pristine MMS (Fig. 3 and Table 3) evidence the presence of a major content in plagioclase, mainly attributed to andesine, and 14 wt% of pyroxene, equally distributed between the detected augite and pigeonite phases. Orthoclase, olivine, montmorillonite, and a small amount (3 wt%) of an amorphous phase were also found, along with a phase with the Fd-3m special group, attributed to cobalt iron oxide (Table 3). The montmorillonite phase presents a stacking fold layer disposition, that was fitted using the Ufer Model.

Results obtained in the present study on the composition of MMS simulant generally agree with previous literature findings, with some differences. Indeed, **Peters et al.** [34] also identified plagioclase and pyroxene phases, as well as magnetite and olivine, even though they did not estimate their quantity. More recently, **Clark et al.** [54] performed the quantitative phase analyses of the MMS simulant. The resulting amount of the plagioclase phase was relatively lower (60.7 wt%) and that of pyroxene (20.7 wt%) slightly higher compared to the results obtained in this work and listed in Table 3. Additionally, **Clark et al.** [54] identified the presence of calcite (1 wt%) as well as a high phyllosilicates content (15.6 wt%) in the MMS simulant. Both phases were not indicated by the developers of this regolith simulant [34]. Accordingly, in this work no calcite was detected while a significantly lower quantity of phyllosilicates (3 wt%) was found (Table 3).

Moreover, **Clark et al.** [54] did not report the presence of olivine (4 wt% in our work). As stated by the same authors [54], the analyzed MMS batch was possibly sourced from a chemically altered area of the Saddleback basalt, and this feature provides a plausible justification for such discrepancies.

As for the pristine JSC-Mars-1A, Fig. 3 and Table 3 evidence the presence of a dominant fraction (53 wt%) of an amorphous phase. In addition, large quantities of plagioclase (25 wt%) and pyroxene (18 wt %) were also detected, along with olivine (3 wt%) and magnetite (1 wt %). These results match, from the qualitatively viewpoint (no quantitative analysis was provided), with the mineralogic phases indicated by the vendor [38]. More recently, **Shindler et al.** [33] provided a semi-quantitative analysis of crystalline phases, whereas the relevant amorphous counterpart (Table 3) was completely neglected. Nonetheless, the crystalline phases identified by **Shindler et al.** [33] are consistent with our findings. Given the absence of quantification of the amorphous part, and the higher accuracy provided by the Rietveld refinement compared to semi-quantitative analyses, it can be stated that,

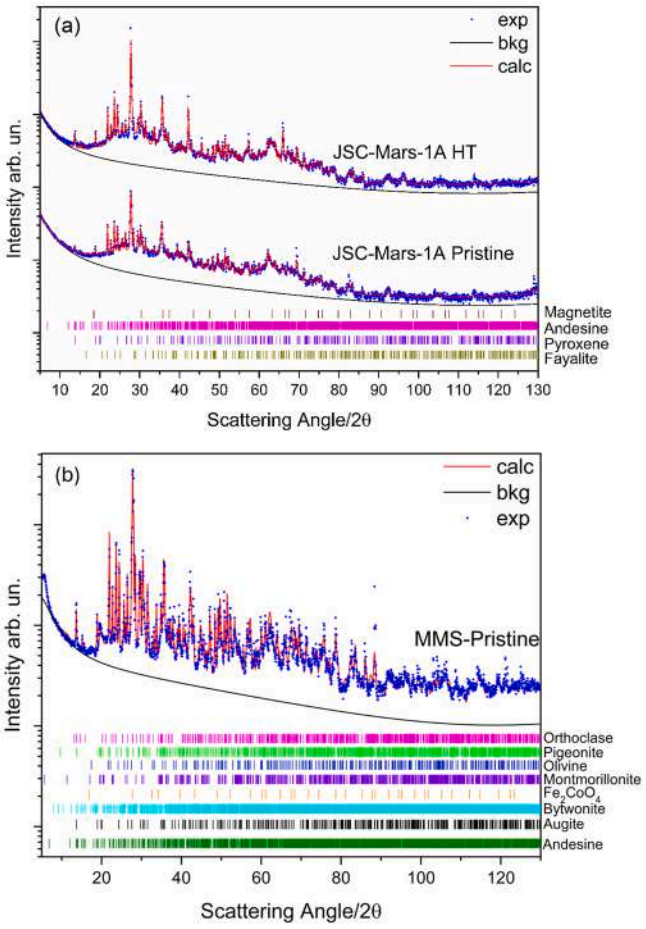

Fig. 3. XRD patterns of (a) JSC-Mars-1A (pristine and heat-treated) and (b) pristine MMS simulants.

Table 3
Phase composition of pristine MMS and JSC-MARS-1A simulants obtained by Rietveld refinement (n.d.: not detected).

Phase	MMS-Pristine (wt. %)	JSC-Pristine (wt. %)	JSC-HT (wt. %)
Amorphous content	3	53	47
Phyllosilicates	3 (**Montmorillonite**)	n.d.	n.d.
Plagioclase	70 (**Andesine**) <1 (**Bytownite**)	25 (**Andesine**)	37 (**Andesine**)
Olivine	4	3 (**Fayalite**)	3 (**Fayalite**)
Pyroxene	8 (**Augite**) 8 (**Pigeonite**)	18	12
Magnetite	n.d.	1	1
K-feldspar	2 (**Orthoclase**)	n.d.	n.d.
Fe_2CoO_4	1	n.d.	n.d.

Table 2
Particle size parameters of Martian regolith simulants used to produce bulk samples.

	JSC-Mars-1A	MMS
d10 [μm]	2.04 ± 0.33	2.52 ± 0.09
d50 [μm]	23.85 ± 1.06	23.38 ± 0.95
d90 [μm]	57.39 ± 4.03	65.92 ± 2.69
d [4,3] [μm]	27.18 ± 1.55	29.40 ± 1.22

Density of the pristine (MMS) and heat treated (JSC-Mars-1A) simulants measured by pycnometer are about 2.77 and 2.84 g/cm^3, respectively.

compared to **Shindler et al.** [33], the data reported in this work more closely mimic the actual phase composition of the simulant.

Table 3 also evidences the fact that the amorphous fraction in the JSC-Mars-1A system is reduced from 53 to 47 wt% because of the heat treatment received. Correspondingly, the content of crystalline phases, in particular plagioclase, increased from 25 to 37 wt%.

3.2. Spark Plasma Sintering of regolith simulants

The sintering behavior of MMS (pristine) and JSC-Mars-1A (preliminarily heat treated at 700 °C) simulants can be deduced from the corresponding SPS outputs, namely sample shrinkage, and gas pressure inside the chamber, reported in Fig. 3 for experiments performed at T_D = 1000 °C and P = 15 MPa.

It is apparent that the two simulants behave quite differently during the SPS test conducted under the same conditions. First, the final value of sample shrinkage (δ) for the JSC-Mars-1A system resulted to be about three times higher than that recorded for MMS. Such discrepancy is consistent with the relative densities of the resulting sintered samples, equal to 99.3 and 76.5% for JSC-Mars-1A and MMS, respectively. In addition, the densification of the latter one is observed to occur very gradually, at a low rate, until the T_D value is achieved. In contrast, sample shrinkage increased very rapidly, particularly in the temperature range of 200-900 °C, when the JSC-Mars-1A simulant was processed. Given the broader sintering window and lower temperatures required for the consolidation of JSC-Mars-1A, the effect of the dwell temperature on sample density was investigated in the range of 800-1000 °C for this system. On the other hand, this study was conducted in the range of 950-1050 °C when considering the MMS counterpart.

The observed differences in the sintering behavior could be primarily imputable to the diverse composition of the two simulants. In particular, as reported in Fig. 3 and Table 3, JSC-Mars-1A is dominated by the amorphous fraction, which highly promotes sample densification, while MMS basically consists of crystalline phases such as andesine and pyroxenes.

The P curves reported in Fig. 4 indicate that the gases release, starting to occur inside the SPS chamber at about 100 °C, is more evident with JSC-Mars-1A. Such phenomenon can be likely attributable to the evaporation of the adsorbed water in both systems.

The effect of the dwell temperature and the applied pressure on product densification was investigated. Fig. 5(a) and 5(b) underline the positive effect of both parameters on the final densities of JSC-Mars-1A and MMS specimens, respectively. As for the JSC-Mars-1A, fully dense samples are obtained at 1000 °C/30 MPa. In this regard, it should be

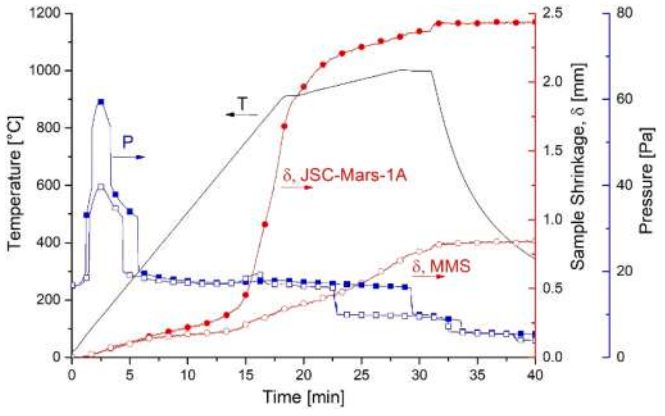

Fig. 4. SPS outputs (sample shrinkage, gas pressure inside the sintering chamber) and the corresponding temperature time profile recorded during the consolidation of JSC-Mars-1A (preliminarily heat treated) and pristine MMS regolith powders for the case of T_D = 1000 °C, P = 15 MPa. Filled and empty symbols refer to JSC-Mars-1A and MMS, respectively.

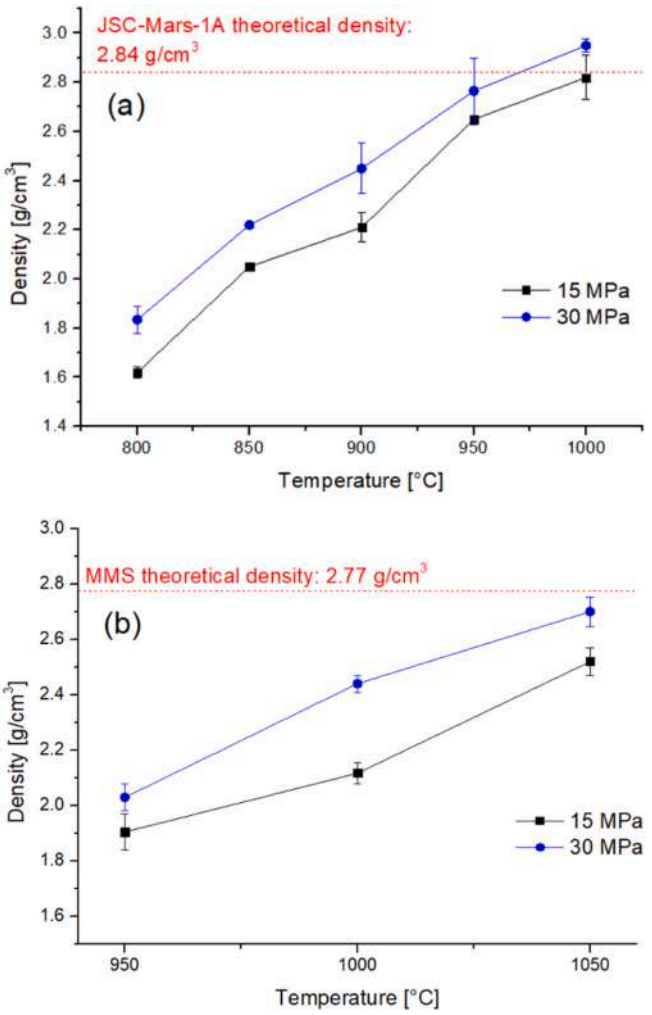

Fig. 5. Effect of the dwell temperature, at different mechanical pressure levels, on the density of bulk samples obtained by SPS from (a) JSC-Mars-1A (preliminarily heat-treated) and (b) pristine MMS regolith simulants.

noted that the measured density of certain samples obtained under such SPS conditions exceeded the theoretical value. This can be ascribed to the fact that the latter one refers to the starting simulant. However, as discussed afterwards, crystallization phenomena occurred on the JSC-Mars-1A sample during SPS, with consequent compositional/structural modifications, so that the theoretical density of the material is expected to change.

From the thermal cycling tests carried out on representative sintered samples in the range from −80 °C to RT, neither damage nor cracks formation were evidenced (Fig. 6a and b). This finding testifies the capability of JSC-Mars-1A and MMS samples to resist the temperature changes taking place on the planet during each sol.

3.3. Compositional, and microstructural characterization

Compositional and structural changes occurring when JSC-Mars-1A regolith was processed by SPS under different conditions can be deduced from the related XRD patterns shown in Supplementary Fig. S3. The amount of each phase estimated by Rietveld refinement are plotted in Fig. 7 and summarized in Table 4, while crystallite size, microstrain, and lattice parameters are reported in Supplementary Tables S1, S2 and S3, respectively. Fig. 7 shows that, during SPS, the amorphous fraction in the simulant progressively decreased down to 16 wt% as the dwell temperature was augmented up to 1000 °C. Correspondingly, the content of both andesine and, at a lower degree, pyroxene increases up to 57

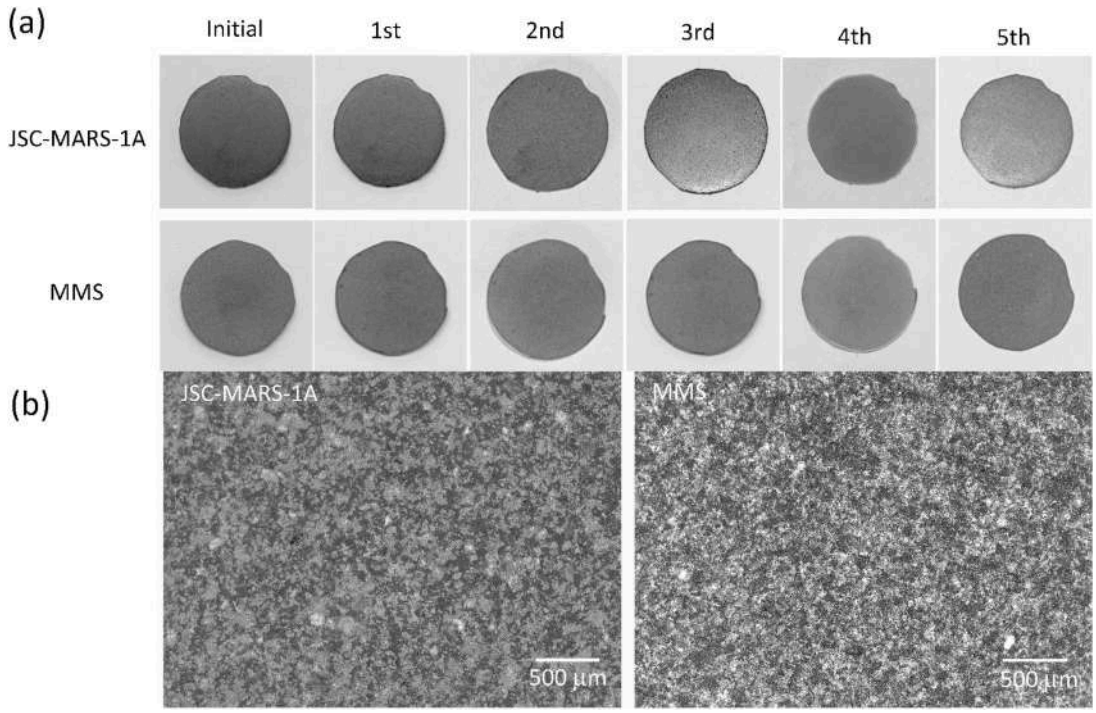

Fig. 6. (a) Optical images showing no noteworthy changes occurring on JSC-Mars-1A and MMS samples after each thermal cycling test (five cycles) conducted in the range from −80 °C to RT; (b) detailed views of the samples after the 5th cycle showing no cracks formation.

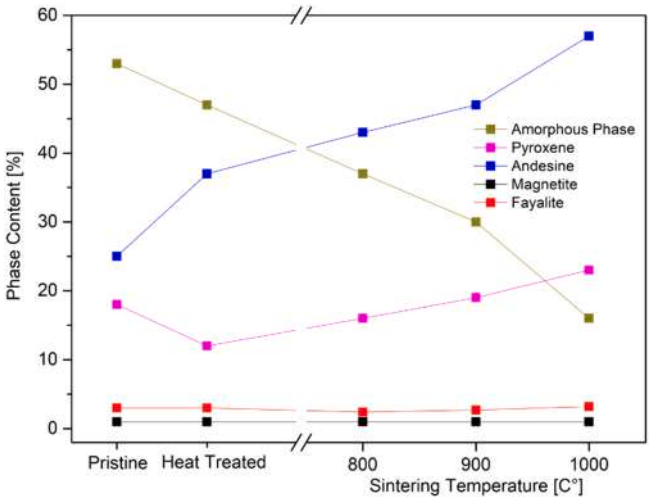

Fig. 7. Phase content changes, as determined by Rietveld analysis from XRD patterns (Supplementary Fig. S3), of JSC-Mars-1A regolith samples after heat treatment at 700 °C and during SPS at T_D = 800, 900, and 1000 °C with respect to the pristine simulant.

and 23 wt%, respectively. On the other hand, the relative amount of fayalite and magnetite remained nearly the same. As reported in Supplementary Table S1, crystallite size of the different phases tends to increase as the SPS condition became progressively more severe.

In contrast with the behaviour displayed by JSC-Mars-1A regolith, the significantly lower content of the amorphous phase makes the MMS counterpart much more thermally stable. This is testified by the minor changes, with respect to the pristine simulant, in the XRD patterns of the samples produced at different SPS conditions (Supplementary Fig. S4). This feature is even clearer when observing the corresponding phases' amounts plotted in Fig. 8 (see also Table 4 for a summary). The most considerable, but still limited, phase transition phenomenon is the disappearance of the montmorillonite phase, originally present in the pristine material, in the sample sintered at 950 °C. In conclusion, it is possible to state that, apart from other minor oscillations, phases originally present in the MMS simulant preserve their quantitative distribution along the entire SPS experimental campaign.

3.4. Morphological-roughness characterization and thermal conductivity estimation

Based on the results obtained in previous sections, three SPS conditions have been selected for each simulant to produce the SPS samples to be subjected to optical measurements. Specifically, the JSC-Mars-1A specimens obtained at 800 °C/15 MPa (JSC@800-15), 900 °C/30 MPa (JSC@900-30), and 1000 °C/30 MPa (JSC@1000-30), were considered to cover a quite wide relative density range, i.e. from 57 to >99.9%. For the same reason, the MMS samples obtained at 950 °C/30 MPa (MMS@950-30), 1000 °C/30 MPa (MMS@1000-30), and 1050 °C/30 MPa (MMS@1050-30), were selected.

SEM images reported in Fig. 9 show the morphological differences on the surface of JSC-Mars-1A and MMS samples sintered at different conditions which will be further characterized from the optical viewpoint. In particular, the JSC@800-15 sample (57% dense) appears to be poorly consolidated, suggesting that the sintering process is in its early stage. On the other hand, JSC@900-30 (86.3% dense) and, especially, JSC@1000-30 (>99.9% dense) products are highly densified. As for the MMS simulant, Fig. 9 shows a different scenario.

Indeed, with reference to Fig. 9, even if a progressive densification improvement is achieved as sintering temperature was augmented, bulk MMS samples appear to be less compacted, compared to the JSC-Mars-1A ones, even at the most severe conditions adopted for this system (1050 °C/30 MPa). Thus, consistently with density data reported in Fig. 5(a) and 5(b) the MMS system clearly exhibits a more refractory nature with respect to the other simulant.

Since surface porosity and roughness characteristics are expected to affect the optical properties of the bulk samples, these properties have been measured. The obtained results are reported in Tables 5, and

Table 4
Phase composition of sintered JSC-Mars-1A and MMS simulants estimated by Rietveld refinement (n.d.: not detected).

Sample ID	Amorphous content (wt. %)	Plagioclase (wt.%)	Pyroxene (wt.%)	Olivine (wt. %)	Orthoclase (wt. %)	Magnetite(wt. %)	Other (wt. %)
JSC@800-15	37	43 (Andesine)	16	2.4 (Fayalite)	n.d.	1	n.d.
JSC@900-30	30	47 (Andesine)	19	2.7 (Fayalite)	n.d.	1	n.d.
JSC@1000-30	16	57 (Andesine)	23	3.2 (Fayalite)	n.d.	1	n.d.
MMS@950-30	3	71 (Andesine) + 1 (Bytownite)	8 (Augite) + 10 (Pigeonite)	2	2	n.d.	3 (Fe_2CoO_4)
MMS@1000-30	2	74 (Andesine) + 1 (Bytownite)	5 (Augite) + 10 (Pigeonite)	1	3	n.d.	4 (Fe_2CoO_4)
MMS@1050-30	2	76 (Andesine) + 1 (Bytownite)	8 (Augite) + 7 (Pigeonite)	1	1	n.d.	4 (Fe_2CoO_4)

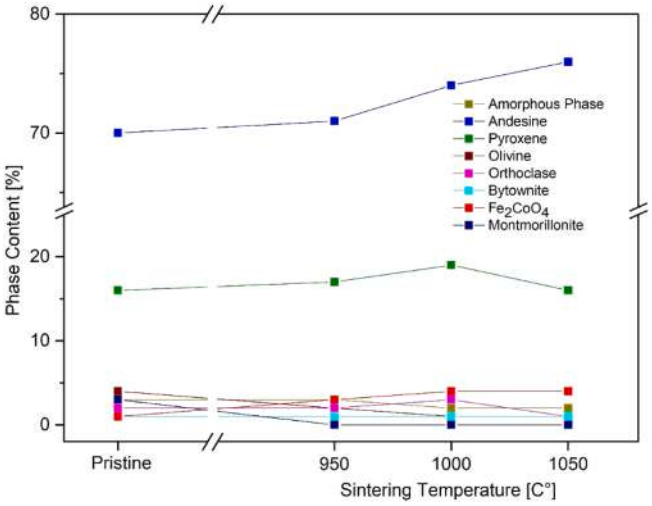

Fig. 8. Phase content changes, as determined by Rietveld analysis from XRD patterns (Supplementary Fig. S4), of MMS regolith samples during SPS at T_D = 950, 1000, and 1050 °C with respect to the pristine simulant.

Table 6, respectively. The obtained values confirmed the trend showed by the SEM images (Fig. 9). In particular, the MMS@1050-30 sample resulted to be rougher and more porous than the JSC@1000-30 one.

It should be noted that some surface pores observed in bulk samples of both systems (Fig. 9(a) and 9(b)) are due to grain pulling-out generated during the polishing procedure. Therefore, the surface porosity seen in Fig. 9(a) and 9(b) is not representative of the actual densification levels achieved during the SPS process, which are significantly higher.

The estimated thermal conductivities of the different JSC-Mars-1A and MMS sintered samples are listed in Table 7 along with data reported in the literature for regolith-like materials.

It should be noted that the only experimental measurements of this property on sintered Martian regolith were carried out by **Deng et al. 2025** [55]. Thus, the results obtained in the latter study have been used to validate the modelling approach adopted in the present work to estimate thermal conductivity. As reported in Table 7, the measured and calculated values are in reasonably good agreement, particularly for highly dense samples, i.e. 3.08 and 3.02 W/mK, respectively. When considering JSC-Mars-1A and MMS systems, composition and porosity data reported in Tables 4 and 5, respectively, were used to estimate the thermal conductivity of the different samples. As expected, the resulting k values monotonically increased as samples' porosity was progressively reduced. In particular, the most conductive sample resulted to be JSC@1000-30, (k = 2.27 W/mK). The relatively higher k values reported in [55] can be readily ascribed to the different composition of the diverse Martian simulants investigated, being the one used by **Deng et al. 2025** [55] richer in more conductive pyroxene and olivine constituents [45]. Nonetheless, the results obtained in this work are in line with values reported in the literature for similar sintered materials or basaltic rocks.

3.5. Optical properties

Preliminarily, optical properties were assessed for the powdered simulants, whose hemispherical reflectance spectra are shown in Fig. 10. The spectrum of untreated JSC-Mars-1A fairly agrees with the available literature data in the range 0.4-2.2 μm wavelength for the similar JSC-Mars-1 simulant **[60]**. As for MMS, our measured reflectance also agrees with available spectra of MMS-2 in the UV-visible-Near-IR [60]. The thermally treated JSC powder shows a considerably increased reflectance with respect to the untreated one (Fig. 10). In agreement with published data [34,61], MMS powders are characterized by a higher reflectance than pristine JSC-Mars-1A in the visible-NIR, even if still lower than that of the heat-treated simulant. The highest reflectance for wavelengths longer than 3 μm is shown by MMS. Pristine simulants and both JSC-Mars-1A samples' curves are characterized by a relatively featureless ferric absorption edge through the visible, an indication of a ferric absorption band around 0.8-0.9 μm (more pronounced in MMS), and relatively flat absorption in the near-IR, except for the bands around 1.4 and 1.9 μm (less intense in MMS), which can be ascribed to OH and H_2O, which are not expected in real Mars regoliths [62] due to the much drier planetary environment.

Before further describing and discussing the optical properties of such simulants, it should be briefly recalled, as mentioned in the Introduction, that the latter ones have been recognized to be representative of real Mars surface. Indeed, unlike the Moon, no sample return mission has been carried out to Mars to date. Therefore, real Mars regoliths are not currently available to be used as benchmarks for the same characterization. Additional considerations regarding the reliability of these simulants to properly mimic the whole actual Martian soil characteristics are beyond the scope of this work.

Besides, it is known that the surface of the planet is not homogeneous, so that several simulants have been, and still are being, developed to reproduce specific properties of Mars surface, as new sites of interest are identified or more data become available [54,61], as well as to replicate the mineralogical content of some Mars meteorites [55,64].

As for optical properties, the simulants here investigated are considered as a valid approximation for specific planet locations. For instance, JSC-Mars-1 (of which JSC-Mars-1A is the second produced batch) is recognized to simulate well the bright regions on the surface [60], as well as to reproduce the chemical composition of regoliths analyzed in the course of the Viking lander, Mars and Spirit Rover missions [19]. As for the MMS simulant, a similar version named MMS-2 is recognized to offer a good match with the observations of the NOMAD instrument on the ExoMars 2016 Trace Gas Orbiter taken at the Elysium Planitia in clear sky conditions and available in the 400–600 nm wavelength range [60].

Fig. 11 shows the reflectance spectra of the ceramics sintered at various temperatures, and those of the corresponding powders. Despite the different absolute values in the spectral region below 8 μm between JSC-Mars-1A (Fig. 11(a)) and MMS-based (Fig. 11(b)) samples, the two

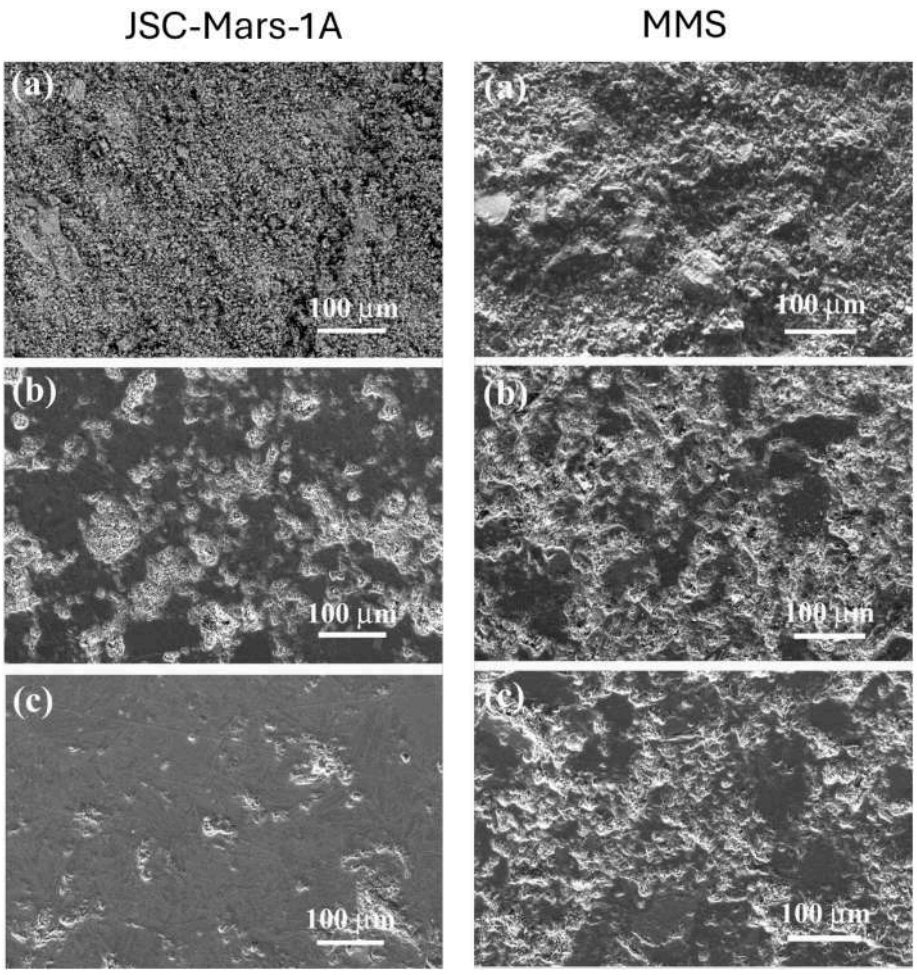

Fig. 9. SEM micrograph of SPS samples obtained from the two regolith simulants. JSC-Mars-1A-based pellets are shown in the first column: (a) JSC@800-15, (b) JSC@900-30, and (c) JSC@1000-30; MMS-based ones in the second column: (a) MMS@950-30, (b) MMS@1000-30, and (c) MMS@1050-30.

Table 5
Average values and standard deviation of surface porosity measured by image analysis on bulk JSC-Mars-1A and MMS samples sintered at different conditions.

Simulant	Sample ID	T_D (°C), P (MPa)	Porosity (vol. %)
JSC-Mars-1A	JSC@800-15	800 °C, 15 MPa	38.15 ± 5.76
	JSC@900-30	900 °C, 30 MPa	24.19 ± 9.17
	JSC@1000-30	1000 °C, 30 MPa	5.47 ± 1.59
MMS	MMS@950-30	950 °C, 30 MPa	39.86 ± 7.10
	MMS@1000-30	1000 °C, 30 MPa	34.47 ± 10.48
	MMS@1050-30	1050 °C, 30 MPa	12.69 ± 4.23

Table 6
Average values and standard deviation of roughness parameters measured on the bulk JSC-Mars-1A and MMS samples obtained at different SPS conditions.

Simulant	Sample ID	Ra [µm]	Rz [µm]	Rq [µm]
JSC-Mars-1A	JSC@800-15	10.05 ± 1.03	86.26 ± 9.24	12.86 ± 1.35
	JSC@900-30	1.19 ± 0.08	17.85 ± 3.19	1.78 ± 0.20
	JSC@1000-30	0.48 ± 0.07	12.70 ± 3.33	0.90 ± 0.18
MMS	MMS@950-30	10.49 ± 2.47	84.16 ± 27.66	13.71 ± 3.51
	MMS@1000-30	2.01 ± 0.13	20.45 ± 2.74	2.66 ± 0.19
	MMS@1050-30	1.21 ± 0.09	14.27 ± 2.21	1.73 ± 0.13

groups show a qualitatively similar behavior. As the sintering temperature is augmented, the reflectance decreases for wavelengths lower than 8 µm, while it increases for longer wavelengths. Sintered samples have a generally lower reflectance than the starting powders in the spectral range below 8 µm, whereas its value becomes higher above this wavelength.

If the spectra of sintered pellets are concerned, it should be observed that optical properties of ceramic bulks depend on several parameters: chemical composition, phases occurring and their relative amounts, total porosity, pore size, grain size, grain crystallographic orientation, and surface roughness. However, among them, the primary parameters affecting optical properties of ceramics for solar applications on Earth have been identified to be the chemical and phase composition [65,66]. This seems to provide a reasonable explanation for the differences shown in the spectral shapes of curves in Fig. 11, also considering the opposite trends shown by the curves for wavelengths below and above 8 µm as a function of the sample density. However, surface features like roughness and porosity, here given in Tables 5 and 6 as pure informative data to more precisely identify the samples, estimate the thermal conductivity (for porosity) and as a term of comparison for future investigations, will be useful degrees of freedom to further optimize optical properties [67], once the most promising composition/processing technique has been identified, similarly to the approach successfully explored for thermal solar absorbers for terrestrial use [68,69].

4. Discussion

Before evaluating the potential of a technological application, it is important to define the framework where it should operate. Mars has

Table 7
Thermal conductivity (k) of JSC-Mars-1A and MMS sintered samples estimated according to Eqs. (1-2). Literature data of similar materials are also reported for the sake of comparison.

Regolith-like material	Sample type; Porosity, γ (vol. %)	Estimated k [W/mK]; T condition	Measured k [W/mK] ; T condition
JSC-Mars-1A	Sintered (JSC@800-15); see Table 5	0.97; RT	-
	Sintered (JSC@900-30); see Table 5	1.44; RT	-
	Sintered (JSC@1000-30); see Table 5	2.27; RT	-
MMS	Sintered (MMS@950-30); see Table 5	0.92; RT	-
	Sintered (MMS@1000-30); see Table 5	1.05; RT	-
	Sintered (MMS@1050-30); see Table 5	1.94; RT	-
BH-Mars-S	Sintered (PSD2-1200 °C); ~10–15	- 2.67; RT	2.70 [55] −100 °C 2.95 [55] ; RT
	Sintered (PSD2-1250 °C); <1%	- 3.02; RT	2.80 [55]; −100 °C 3.08 [55] ; RT
Basalt rock	Rock	-	2.1 [16]; RT 1.5–2.5 [55]; RT
JSC-Mars-1	Powder	- -	~0.01÷~0.10 [56]; RT ~0.07÷~0.12 [57]
MMS	Powder	-	0.03 ÷ 0.07; −30 ÷ 30 °C [58]
Actual, data from InSight Mars mission	Soil (63^{+4}_{-9} %)	-	0.039 ± 0.002 [59]; Actual Martian conditions
Lunar regolith simulant	Sintered Powder	- -	~2.0 [16] 0.01 [16]

both similarities and important differences with respect to Earth [47], as summarized in what follows.

a) the duration of the day/night cycle is similar to the terrestrial one;
b) it has an atmosphere, albeit thinner than that on Earth, mainly consisting of CO_2, N_2, Ar and typically containing a significant amount of suspended dust, which scatters the incoming sunlight;
c) ice is present on the poles which eventually can be used as a source of CO_2 and water;
d) it has a tilted axis, which causes seasons, but they last longer than terrestrial ones, since the Martian year is about twice longer (669.6 sols i.e. Martian days, equivalent to 687 Earth days). Moreover, while terrestrial seasons are evenly spread over the year, on Mars they vary in length because of the more elliptical orbit: spring in the northern hemisphere (autumn in the southern) is the longest season at 194 sols. Autumn in the northern hemisphere (spring in the southern) is the shortest at 142 sols. Northern winter/southern summer is 154 sols, and northern summer/southern winter is 178 sols. Further differences are concerned with the lower solar irradiance on Mars, being farther from the Sun, and the lower surface temperatures ranging from 130 to 300K [70].
e) Finally, dust storms due to winds happen occasionally with a site-dependent occurrence. These phenomena can be local or global, with the latter that can last for weeks and even months. Storms strongly attenuate atmospheric transmission, decreasing the direct solar irradiance on the planet surface while increasing the diffuse component. An extensive database has been built for the optical depth of Mars atmosphere from the data collected from the rovers during several missions (Viking [71], Pathfinder [72], Spirit, Opportunity [73], Curiosity [74], and Perseverance [75]). These data allow to identify the latitudes and seasons where dust storms preferentially occur and, on the other hand, those with the lowest probability. In addition to intensity and light propagation direction, the atmospheric dust modifies the sunlight spectral distribution as well, which, at the planet surface, becomes therefore blue-deficient, enriched in red and IR with respect to the AM0 spectrum. These spectral modifications depend on the dust thickness: the smallest thickness is at high sun angles (mid-day, low latitudes), and for low atmospheric dust content (northern hemisphere summer), while the largest thickness is at low sun angles (early and late in the day) and for high dust content (northern hemisphere winter).

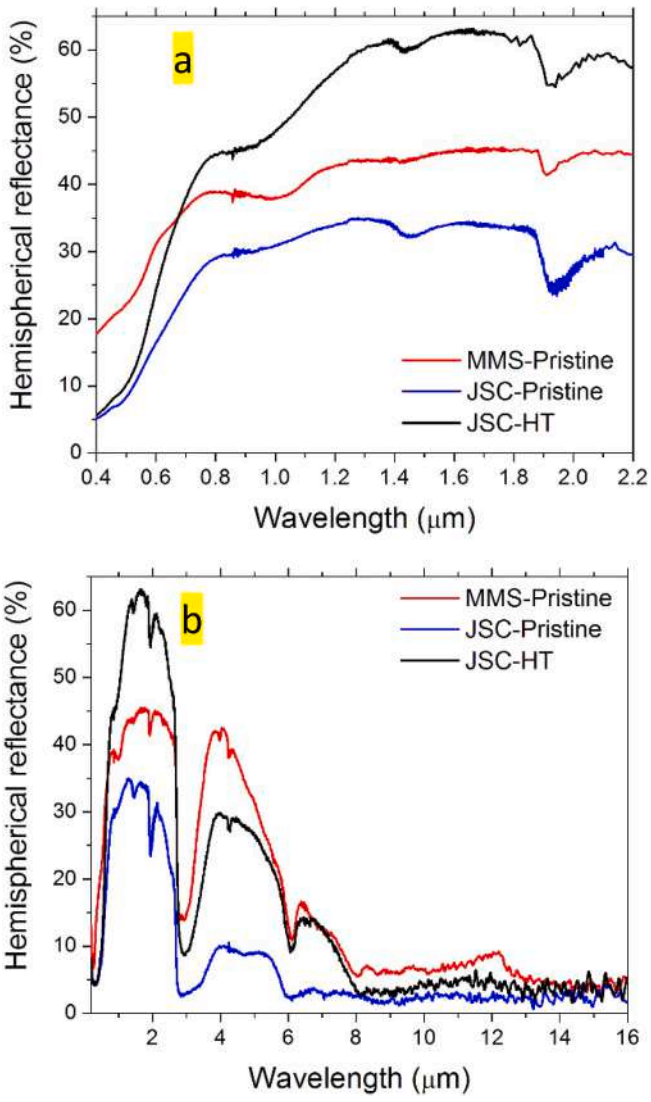

Fig. 10. Reflectance spectra of the simulants in powder form. (a) Spectral range 0.4-2.2 μm, to allow the comparison with Allen et al. [63] and Peters et al. [34]; (b) Full range 0.19-16.0 μm investigated in this work. The experimental uncertainty on the measured values is ±2.

Therefore, due to such a complex scenario, to preliminarily assess the potential of sintered regoliths for solar energy harvest and storage, we have considered, as a case-study, the solar irradiance spectra reported in **Vicente-Retortillo et al.** [76], corresponding to specific conditions

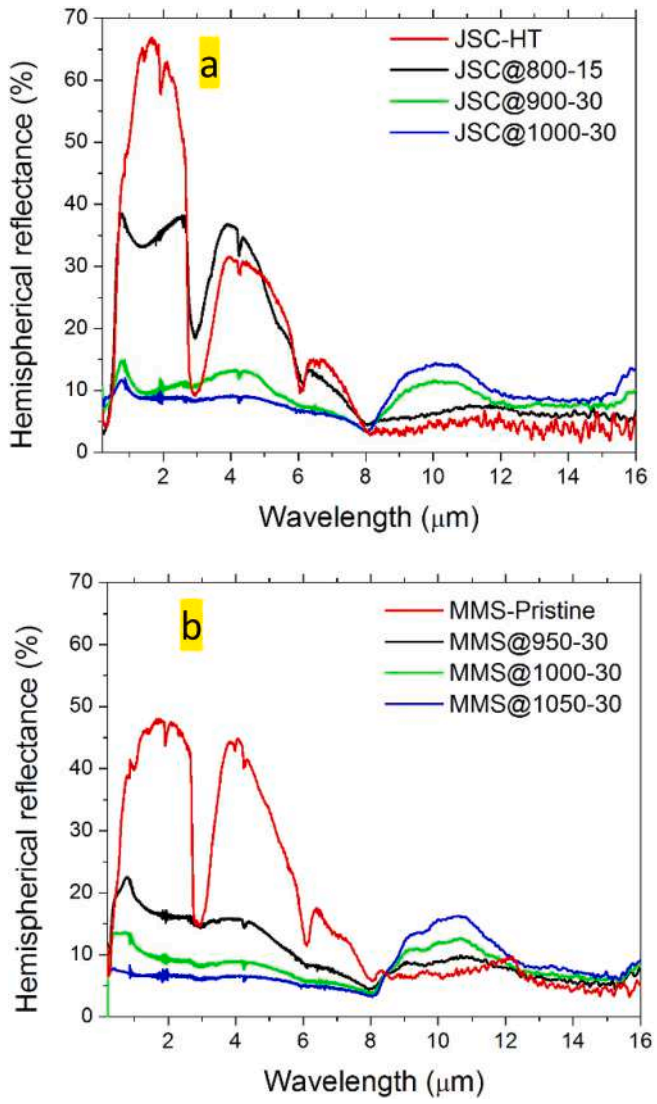

Fig. 11. Reflectance spectra of the sintered ceramics obtained from (a) the JSC-Mars-1 simulant and (b) the MMS simulant. The spectrum of the corresponding powders (the annealed one, in case of JSC-Mars-1 simulant) is also indicated for comparison. The experimental uncertainty on the measured values is ±2.

(latitude = 0°, winter solstice at the northern hemisphere, local noon) and with two values of atmosphere optical depth τ: clear-sky (τ = 0.3) and dusty (τ = 1). The corresponding solar spectra are shown in Supplementary Fig. S5. We calculated the solar absorptance of the materials from Eqs. 1 and 3 considering both the total solar radiation reaching the surface and the direct-only component (i.e. the part of radiation which has not been scattered by the atmosphere). The first case deals with applications where the materials are subjected to non-concentrated solar radiation, like in buildings, to harvest and store heat for habitation or agriculture. The second case deals with applications requiring concentration of solar radiation, i.e. the production of heat at higher temperatures for either thermal use or power production, because the direct component only can be concentrated by optical systems.

Table 8 lists the calculated values of solar absorptance. All the sintered simulants always show a higher solar absorptance than the corresponding powders, with values increasing with the sample density. At the lowest and highest sample densities, the absorptance of MMS-based bulks is superior to that of JSC-based ones, while the reverse is true for the samples with the intermediate density level. The absorptance values of each MMS sintered sample and those of JSC with the highest density are very stable, and do not change either for different conditions of dust

Table 8
Solar absorptance values calculated from Eqs. 3, 5.

Sample	α (total radiation)	α (direct radiation)	α (total radiation)	α (direct radiation)
	Clear Sky		Dusty	
MMS-Pristine	0.70 ± 0.01	0.70 ± 0.01	0.69 ± 0.01	0.70 ± 0.01
MMS@950–30	0.80 ± 0.01	0.80 ± 0.01	0.80 ± 0.01	0.80 ± 0.01
MMS@1000–30	0.87 ± 0.01	0.87 ± 0.01	0.87 ± 0.01	0.87 ± 0.01
MMS@1050–30	0.93 ± 0.01	0.93 ± 0.01	0.93 ± 0.01	0.93 ± 0.01
JSC-HT	0.72 ± 0.01	0.73 ± 0.01	0.72 ± 0.01	0.74 ± 0.01
JSC@800–15	0.75 ± 0.01	0.75 ± 0.01	0.74 ± 0.01	0.75 ± 0.01
JSC@900–30	0.88 ± 0.01	0.89 ± 0.01	0.88 ± 0.01	0.89 ± 0.01
JSC@1000–30	0.90 ± 0.01	0.90 ± 0.01	0.90 ± 0.01	0.90 ± 0.01

in the atmosphere nor if we consider direct or total radiation. Conversely, for the lowest and mid density JSC-Mars-1A-based ceramics, and for both powders as well, some small differences (lower than 1%) in absorptance have been found depending on the dust conditions or the total or direct solar radiation. Overall, both dense samples show a remarkable solar absorptance of 0.90 (JSC-Mars-1A) and 0.93 (MMS), compared with that of powders (0.69-0.70 and 0.72-0.74 only, respectively), showing the potential of using sintered bodies for solar heat production.

These noteworthy values are maintained for both total radiation and the direct component, proposing them to be used for absorption of non-concentrated solar radiation, for instance as construction material or residential solar heat collectors (similar to the concept of residential thermal solar panels on Earth), as well as energy-production material in solar-concentrating systems. As a term of comparison, it should be mentioned that optimized solar-selective surfaces for flat-panels solar collectors on Earth (TiNOX® Energy, Almeco) show a solar absorptance of 0.94 [77], fully comparable to the value of our MMS dense bulk, which, however, still has to be optimized.

Fig. 12 shows the samples' thermal emittance, estimated using Eqs. (3), (4) and (6) in the temperature range 100-600 K (see Fig. S6 in Supplementary for the normalized spectral distributions of blackbody radiation superimposed to emittance spectra). Below 300 K, which is the maximum temperature naturally occurring on the Martian surface [70], higher (JSC-Mars-1A) or comparable (MMS) emittance with respect to sintered simulants can be found in the powders, which, interestingly, also displayed the lowest solar absorptance. Conversely, the samples with the highest solar absorptance values are also characterized by the lowest emittance. This combination of properties is very promising for converting solar radiation into heat, as the highest efficiency in collection (high α value) is merged to the lowest thermal losses by radiative effects (low ε). Such finding proves the promising approach, for energy applications and within the ISRU perspective, of sintering planetary regolith to produce materials with radically different properties with respect to the pristine ones. At higher temperatures, the emittance of these simulants increases with temperature up to about 1% (JSC-Mars-1A) and 2% (MMS) at most, with overall values between 0.90 and 0.95. This makes them promising candidates for radiating materials (e.g. in radiating furnaces or in other applications, where the controlled heat release is required). As for the powders, emittance monotonically drops to 0.84 (JSC-Mars-1A) and 0.80 (MMS), making them more suited as heat storage media. The lowest-density JSC-Mars-1A specimens show an emittance temperature trend similar to that of starting powders, albeit with a lower emittance, which similarly potentially qualifies them for thermal energy storage applications.

For the mentioned applications, a key parameter is thermal conductivity. Table 7 lists the literature values for some Mars and Lunar regolith simulants, either in powder or bulk forms, together with the values for our sintered samples, estimated from Eq. (1.2). It is known that thermal conductivity is affected by several factors besides composition, including particle size (for powders), porosity and atmospheric pressure. Typically, thermal conductivity **k** of bulk solids is higher than

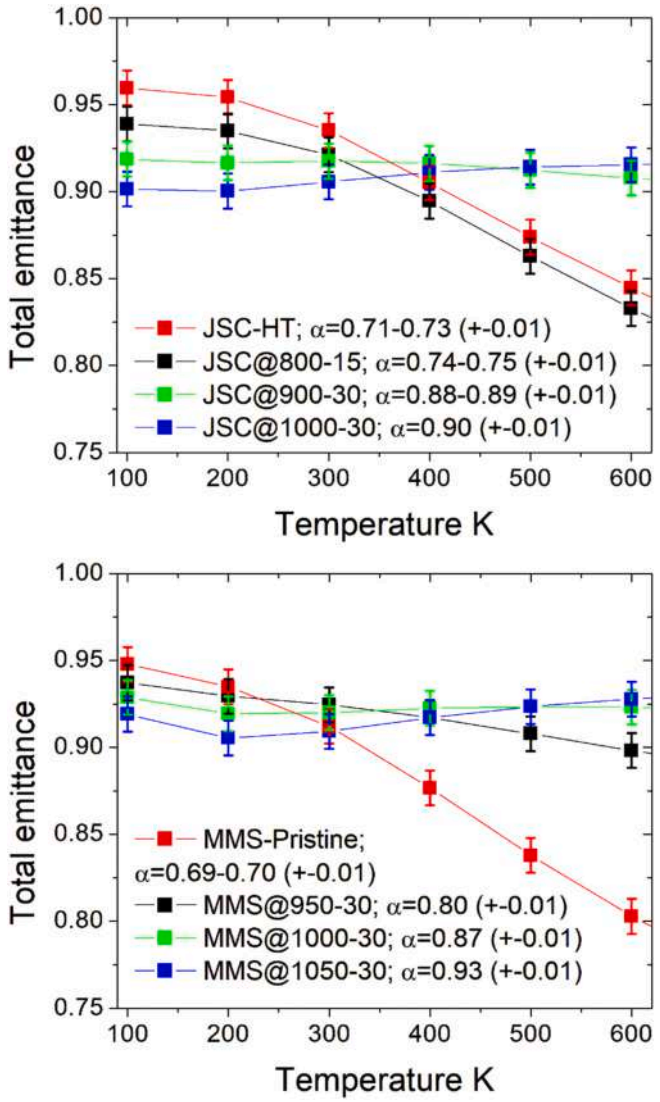

Fig. 12. Total emittance calculated from normal hemispherical reflectance spectra (Eqs. (3), (4) and (6)).

that of powders, this property decreases with sample porosity, and, for porous solids, higher ambient pressures entail higher **k**. For sintered Lunar regolith simulants, it has been shown a 200-fold increase in thermal conductivity for sintered ceramics with respect to the original powders [16].

From Table 7, we can see that the considered powdered simulants, which have different compositions, all show a thermal conductivity of the order of magnitude of few 10^{-2} W/mK, reaching values around 10^{-1} W/mK for higher pressures. On the other hand, as discussed above, the estimated values for our sintered pellets fairly agree with the literature values for thermal conductivities of sintered Mars and Lunar simulants, considering the differences in mineral compositions occurring among the samples found in the literature. Therefore, our experimental results on optical properties, associated with the estimated data on thermal conductivity, confirm the high ISRU potential of regoliths as well as the high level of property manipulation and optimization supplied by the parameters of the sintering process.

Notably, such property tunability translates into application flexibility, a highly desirable characteristic within ISRU. For instance, when thermal insulation is needed (e.g., in lining habitat walls, or in insulation structures around thermal batteries), regolith should be used as powder or porous solid. In order to supply the needed level of thermal comfort to the interior of habitats, this property should be combined with a high thermal emittance. On the contrary, insulation of thermal batteries requires low thermal emittance to reduce radiation losses. Still in the field of buildings application, the exterior of habitats should feature a high solar absorptance, which fits with the characteristics of dense sintered regoliths. Similarly, to maximize the thermal solar energy harvest and the efficient transfer to the storage medium, the high solar absorptance and thermal conductivity of dense pellets should be considered. In addition, the storage of sensible heat into a thermal mass would benefit from low thermal emittance combined with high thermal conductivity, to reduce losses and to have an efficient charge/discharge, respectively.

5. Conclusions

Two Martian regolith simulants with different compositional/structural properties are investigated in this work to evaluate the possible use of *in-situ* available similar materials for future manned missions on Mars. To strongly reduce the organic species and water originally present in JSC-Mars-1A, thus better mimicking the actual Martian regolith characteristics, the latter one required a pretreatment at 700 °C. Such simulant consisted of a dominant amorphous phase (53 wt%), which is reduced (47%) after the pretreatment stage, whereas MMS is basically constituted of crystalline phases (mainly andesine). Such discrepancies, which are representative of the wide spectrum of soils available on the Mars surface, are responsible for the quite different behavior manifested by the two simulants when processed by SPS to produce bulk samples. Specifically, the MMS system exhibits a relatively higher refractory character, with the related powders being properly consolidated (up to 97.5 % relative density) only at dwell temperature of 1050 °C. Correspondingly, no marked compositional changes occurred. In contrast, fully dense samples are obtained by SPS from JSC-Mars-1A at 1000 °C with a significant reduction of the amorphous fraction (down to 16 wt%) and the concurrent increase in the amount of crystalline andesine and pyroxene.

The optical properties of the two systems have been determined by examining bulk specimens with diverse characteristics produced by SPS under different conditions. The sintering process drastically changed the optical spectra. The values of optical parameters, i.e. solar absorptance and thermal emittance, useful to assess the materials potential for thermal solar energy conversion, have been evaluated in an exemplifying case (0° lat., winter solstice at the northern hemisphere, local noon), both in clear sky and dusty conditions. Very interestingly, the bulk specimens showed a significantly higher solar absorptance than the corresponding powders, with a remarkable value of 0.93 for the densest MMS sample. As a term of comparison, it is worth to note that this value is approaching that of one of the most advanced thermal solar absorber material available in thermal solar collectors for terrestrial building market to date (TiNOX® Energy, Almeco). At the same time, the thermal emittance of ceramics is lower than that of powders for temperatures below ~300K, and superior for higher levels, with values which remain quite stable in the whole investigated temperature range. Various possible outdoor and indoor applications have been discussed, with reference to the different combinations of functional properties obtainable. Overall, our study, linking energy-related functional properties to sintering process parameters, proves that sintered and powder regoliths can be synergistically used for solar energy harvesting, heat production, storage and release, as well as for buildings application, within the ISRU perspective.

CRediT authorship contribution statement

Mariano Casu: Writing – review & editing, Visualization, Investigation, Data curation. **Roberto Orrù:** Writing – review & editing, Writing – original draft, Supervision, Methodology, Conceptualization. **Roberta Licheri:** Writing – review & editing. **Alessandro Concas:** Writing – review & editing. **Giacomo Cao:** Writing – review & editing.

Costantino Cau: Investigation. **Sebastiano Garroni:** Writing – review & editing, Investigation. **Aldo Dell'Oro:** Writing – review & editing, Methodology, Investigation. **Elisa Sani:** Writing – review & editing, Writing – original draft, Visualization, Methodology, Investigation, Data curation, Conceptualization.

Declaration of competing interest

The authors declare that they have no known competing financial interests or personal relationships that could have appeared to influence the work reported in this paper.

Acknowledgments

Mariano Casu performed his activity in the framework of the Ph.D. in Innovation Sciences and Technologies at the University of Cagliari, Italy. This work has been developed within the framework of the project e. INS-Ecosystem of Innovation for Next Generation Sardinia (cod. ECS 00000038) funded by the Italian Ministry for Research and Education (MUR) under the National Recovery and Resilience Plan (NRRP)—MISSION 4 COMPONENT 2, "From research to business" INVESTMENT 1.5, "Creation and strengthening of Ecosystems of innovation" and construction of "Territorial R&D Leaders". The "SMS—Space Manufacturing in-situ—Realizzazione in contesti spaziali di manufatti" project (cod. ARS01_01361), sponsored by the Italian Ministry of Education, University and Research, Italy (Cod. CUP: B25F21001330005), is also acknowledged. A part of this activity has been carried out within the framework of the Extended Partnership Space It Up!, Spoke 1, funded by the Italian Space Agency (ASI) and the Ministry of University and Research (MUR). Contract n. 2024-5-E.0 – CUP n. I53D24000060005. Aldo Dell'Oro has been supported by a grant of the Italian National Institute for Astrophysics for fundamental research projects (INAF, act n. 38/2023). The authors thank Dr. Luther Beegle (Jet Propulsion Laboratory, Pasadena, USA) for providing the Mojave Martian Simulant, Mr. Mauro Pucci, Mr. Marco Raffaelli and Mr. Andrea Sordini (CNR-INO) for technical assistance, Mrs. Roberta Parenti and Mrs. Antonella Alessi (CNR-INO) for administrative assistance. The technical support of MR. Giovanni Perra, Ph.D. student in Innovation Sciences and Technologies at the University of Cagliari, Italy, for performing thermal cycles, is gratefully acknowledged.

Appendix A. Supplementary data

Supplementary data to this article can be found online at https://doi.org/10.1016/j.actaastro.2026.03.043.

References

[1] A. Vernile, The rise of private actors in the space sector. Springer Briefs in Applied Sciences and Technology, Springer, Cham, 2018, https://doi.org/10.1007/978-3-319-73802-4.
[2] A. Meurisse, J. Carpenter, Past, present and future rationale for space resource utilisation, Planet. Space Sci. 182 (2020) 104853, https://doi.org/10.1016/j.pss.2020.104853.
[3] P.H. Smith, M. Lemmon, Opacity of the Martian atmosphere measured by the Imager for Mars Pathfinder, J. Geophys. Res. Planets 104 (E4) (1999) 8975–8985, https://doi.org/10.1029/1998JE900017.
[4] SpaceX, Mars and beyond: the road to making humanity multiplanetary. https://www.spacex.com/humanspaceflight/mars/. (Accessed 18 April 2025).
[5] J. Vago, O. Witasse, H. Svedhem, et al., ESA ExoMars program: the next step in exploring Mars, Sol. Syst. Res. 49 (2015) 518–528, https://doi.org/10.1134/S0038094615070199.
[6] K.A. Farley, K.H. Williford, K.M. Stack, et al., Mars 2020 mission overview, Space Sci. Rev. 216 (2020) 142, https://doi.org/10.1007/s11214-020-00762-y.
[7] Y. Zou, Y. Zhu, Y. Bai, et al., Scientific objectives and payloads of Tianwen-1, China's first Mars exploration mission, Adv. Space Res. 67 (2) (2021) 812–823, https://doi.org/10.1016/j.asr.2020.11.005.
[8] G.B. Sanders, M. Duke, et al., Capability road map (CRM) 13: in-situ resource utilization (ISRU), in: R. Willcoxon, H. Thronson, G. Varsi, R. Mueller, V. Regenie, T. Inman, et al. (Eds.), NASA Capability Roadmaps Executive Summary, 2005, pp. 264–291. https://ntrs.nasa.gov/citations/20050204002. (Accessed 18 April 2025).
[9] D.R. Williams, A crewed mission to mars. https://nssdc.gsfc.nasa.gov/planetary/mars/marsprof.html, 2015. (Accessed 18 April 2025).
[10] NASA Mars architecture steering group, in: Bret G. Drake (Ed.), Human Exploration of Mars Design Reference Architecture 5.0, 2009. http://www.nasa.gov/pdf/373665main_NASA-SP-2009-566.pdf. (Accessed 18 April 2025).
[11] D. Karl, K.M. Cannon, A. Gurlo, Review of space resources processing for Mars missions: martian simulants, regolith bonding concepts and additive manufacturing, Open Ceramics 9 (2022) 100216, https://doi.org/10.1016/j.oceram.2021.100216.
[12] C.C. Allen, K.M. Jager, R.V. Morris, D.J. Lindstrom, M.M. Lindstrom, J. P. Lockwood, Martian soil simulant available for scientific, educational study, Eos Trans. AGU 79 (1998) 405, https://doi.org/10.1029/98EO00309.
[13] R. Licheri, R. Orrù, E. Sani, A. Dell'Oro, G. Cao, Spark plasma sintering and optical characterization of lunar regolith simulant, Acta Astronaut. 201 (2022) 164–171, https://doi.org/10.1016/j.actaastro.2022.09.016.
[14] Y. Liu, T. Shen, X. Lv, G. Zhang, C. Wang, J. Gu, X. Zhang, Q. Wang, X. Chen, X. Quan, W. Yao, Investigation on a lunar energy storage and conversion system based on the in-situ resources utilization, Energy 268 (2023) 126681, https://doi.org/10.1016/j.energy.2023.126681.
[15] Z. Liu, J. Wang, Z. Wang, T. Yan, K. Cheng, J. Xu, J. Qin, Numerical analysis on lunar heat storage system: Multi-objective optimization, heat storage capacity, and thermal insulation performance, J. Energy Storage 59 (2023) 106508, https://doi.org/10.1016/j.est.2022.106508.
[16] P. Fleith, A. Cowley, A. Canals Pou, A. Valle Lozano, R. Frank, P. López Córdoba, R. González-Cinca, In-situ approach for thermal energy storage and thermoelectricity generation on the Moon: modelling and simulation, Planet. Space Sci. 181 (2020) 104789, https://doi.org/10.1016/j.pss.2019.104789.
[17] M.F. Palos, P. Serra, S. Fereres, K. Stephenson, R. González-Cinca, Lunar ISRU energy storage and electricity generation, Acta Astronaut. 170 (2020) 412–420, https://doi.org/10.1016/j.actaastro.2020.02.005.
[18] B. Tillotson, Regolith thermal energy storage for lunar nighttime power, in: AIAA/NASA/OAI Conference on Advanced SEI Technologies, 1991, https://doi.org/10.2514/6.1991-3420.
[19] D. Karl, F. Kamutzki, A. Zocca, O. Goerke, J. Guenster, A. Gurlo, Towards the colonization of Mars by in-situ resource utilization: slip cast ceramics from Martian soil simulant, PLoS One 13 (2018) e0204025, https://doi.org/10.1371/journal.pone.0204025.
[20] G. Corrias, R. Licheri, R. Orrù, G. Cao, Self-propagating high-temperature synthesis reactions for ISRU and ISFR applications, Eurasian Chem.-Technol. J. 13 (3-4) (2011) 137–148, https://doi.org/10.18321/ectj77.
[21] G. Corrias, R. Licheri, R. Orrù, G. Cao, Self-propagating high-temperature reactions for the fabrication of Lunar and Martian physical assets, Acta Astronaut. 70 (2012) 69–76, https://doi.org/10.1016/j.actaastro.2011.07.022.
[22] A. Concas, G. Corrias, R. Licheri, R. Orrù, M. Pisu, G. Cao, Remarks on ISRU and ISFR technologies for manned missions on moon and mars, Eurasian Chem.-Technol. J. 14 (3) (2012) 243–248, https://doi.org/10.18321/ectj120.
[23] B.J. Chow, T. Chen, Y. Zhong, Y. Qiao, Direct formation of structural components using a Martian soil simulant, Sci. Rep. 7 (2017) 317, https://doi.org/10.1038/s41598-017-01157-w.
[24] P.E. Hintze, S. Quintana, Building a lunar or Martian launch pad with in situ materials: recent laboratory and field studies, J. Aero. Eng. 26 (2013) 134–142, https://doi.org/10.1061/(ASCE)AS.1943-5525.0000205.
[25] D. Karl, F. Kamutzki, P. Lima, A. Gili, T. Duminy, A. Zocca, J. Günster, A. Gurlo, Sintering of ceramics for clay in situ resource utilization on Mars, Open Ceram 2 (2020) 100008, https://doi.org/10.1016/j.oceram.2020.100008.
[26] D. Karl, T. Duminy, P. Lima, F. Kamutzki, A. Gili, A. Zocca, J. Günster, A. Gurlo, Clay in situ resource utilization with Mars global simulant slurries for additive manufacturing and traditional shaping of unfired green bodies, Acta Astronaut. 174 (2020) 241–253, https://doi.org/10.1016/j.actaastro.2020.04.064.
[27] L. Karacasulu, D. Karl, A. Gurlo, C. Vakifahmetoglu, Cold sintering as a promising ISRU technique: a case study of Mars regolith simulant, Icarus 389 (2023) 115270, https://doi.org/10.1016/j.icarus.2022.115270.
[28] G. Cao, C. Estournes, J. Garay, R. Orrù (Eds.), Spark Plasma Sintering: Current Status, New Developments and Challenges, Elsevier, 2019.
[29] X. Zhang, S. Gholami, M. Khedmati, B. Cui, Y.-R. Kim, Y.-J. Kim, H.-S. Shin, J. Lee, Spark plasma sintering of a lunar regolith simulant: effects of parameters on microstructure evolution, phase transformation, and mechanical properties, Ceram. Int. 47 (4) (2021) 5209–5220, https://doi.org/10.1016/j.ceramint.2020.10.100.
[30] X.L. Phuah, H. Wang, B. Zhang, J. Cho, X. Zhang, H. Wang, Ceramic material processing towards future space habitat: electric current-assisted sintering of lunar regolith simulant, Materials 13 (2020) 4128, https://doi.org/10.3390/ma13184128.
[31] X. Zhang, M. Khedmati, Y.-R. Kim, Y.-R. Kim, H.-S. Shin, J. Lee, Y.-J. Kim, B. Cui, Microstructure evolution during spark plasma sintering of FJS-1 lunar soil simulant, J. Am. Ceram. Soc. 103 (2020) 899–911, https://doi.org/10.1111/jace.16808.
[32] W. Han, Y. Zhou, F. Dang, C. Zhou, L. Ding, Spark plasma sintering of HUST-1 lunar regolith simulant and its thermal shock resistance properties, Adv. Space Res. 73 (3) (2024) 1992–2003, https://doi.org/10.1016/j.asr.2023.11.027.
[33] M. Schindler, S. Michel, D. Batcheldor, M.F. Hochella, A nanoscale study of the formation of Fe-(hydr)oxides in a volcanic regolith: implications for the understanding of soil forming processes on Earth and Mars, Geochem. Cosmochim. Acta 264 (2019) 43–66, https://doi.org/10.1016/j.gca.2019.08.008.

[34] G.H. Peters, W. Abbey, G.H. Bearman, G.S. Mungas, J.A. Smith, R.C. Anderson, S. Douglas, L.W. Beegle, Mojave Mars simulant - characterization of a new geologic Mars analog, Icarus 197 (2008) 470–479, https://doi.org/10.1016/j.icarus.2008.05.004.
[35] A. Banin, B.C. Clark, H. Wanke, Surface chemistry and mineralogy, in: H.H. Kieffer, B.M. Jakosky, C.W. Snyder, M.S. Matthews (Eds.), Mars, The University of Arizona Press, Tucson, 1992, pp. 594–625.
[36] C.N. Foley, T.E. Economou, R.N. Clayton, W. Dietrich, Calibration of the Mars Pathfinder alpha proton X-ray spectrometer, J. Geophys. Res. Planets 108 (2003) E12, https://doi.org/10.1029/2002JE002018.
[37] R. Rieder, R. Gellert, R.C. Anderson, J. Bruckner, B.C. Clark, G. Dreibus, T. Economou, G. Klingelhoffer, G.W. Lugmair, D.W. Ming, S.W. Squyres, C. d'Uston, H. Wanke, A. Yen, J. Zipfel, Chemistry of rocks and soils at Meridiani Planum from the alpha particle X-ray spectrometer, Science 306 (2004) 5702 1746–1749, https://doi.org/10.1126/science.1104358.
[38] Orbitec, JSC Mars-1A Martian regolith simulant material safety datasheet. https://web.archive.org/web/20160331191710/http://orbitec.com/store/JSC_Mars-1A_Material_Safety_Datasheet.pdf, 2008. (Accessed 18 April 2025).
[39] H.G. Sizemore, M.T. Mellon, Laboratory characterization of the structural properties controlling dynamical gas transport in Mars-analog soils, Icarus 197 (2008) 606–620, https://doi.org/10.1016/j.icarus.2008.05.013.
[40] R. Ulrich, V. Chevrier, J.D. Chittenden, T. Kral, L. Roe, W.M. Keck, Comparison of numerical modeling and temperature records from the mars pathfinder landing site, in: Proceedings of the 38th Annual Lunar and Planetary Science Conference. Lunar and Planetary Science Conference, March. 2007. https://webapp1.dlib.indiana.edu/virtual_disk_library/index.cgi/1185879/FID2088/abstracts/1166.pdf. (Accessed 15 January 2026).
[41] A. Altomare, C. Cuocci, C. Giacovazzo, A. Moliterni, R. Rizzi, QUALX: a computer program for qualitative analysis using powder diffraction data, J. Appl. Crystallogr. 41 (4) (2008) 815–817, https://doi.org/10.1107/S0021889808016956.
[42] S. Graulis, D. Chateigner, R.T. Downs, A.F.T. Yokochi, M. Quirós, L. Lutterotti, E. Manakova, J. Butkus, P. Moeck, A. Le Bail, Crystallography Open Database - an open-access collection of crystal structures, J. Appl. Crystallogr. 42 (4) (2009) 726–729, https://doi.org/10.1107/S0021889809016690.
[43] L. Lutterotti, Total pattern fitting for the combined size-strain-stress-texture determination in thin film diffraction, Nucl. Instrum. Methods Phys. Res. B 268 (2010) 3–4, https://doi.org/10.1016/j.nimb.2009.09.053.
[44] F. Brigaud, G. Vasseur, Mineralogy, porosity and fluid control on thermal conductivity of sedimentary rocks, Geophys. J. Int. 98 (3) (1989) 525–542, https://doi.org/10.1111/j.1365-246X.1989.tb02287.x.
[45] K. Horai, G. Simmons, Thermal conductivity of rock-forming minerals, Earth Planet Sci. Lett. 6 (5) (1969) 359–368, https://doi.org/10.1016/0012-821X(69)90186-1.
[46] D.S. Smith, A. Alzina, J. Bourret, B. Nait-Ali, F. Pennec, N. Tessier-Doyen, K. Otsu, H. Matsubara, P. Elser, U.T. Gonzenbach, Thermal conductivity of porous materials, J. Mater. Res. 28 (17) (2013) 2260–2272, https://doi.org/10.1557/jmr.2013.179.
[47] NASA, Mars facts. https://science.nasa.gov/mars/facts/. (Accessed 18 April 2025).
[48] M.F. Modest, Radiative Heat Transfer, second ed., Academic Press, 2003 https://doi.org/10.1016/B978-0-12-503163-9.X5000-0.
[49] S. Barbarossa, R. Orrù, G. Cao, A. Balbo, F. Zanotto, E. Sani, Optical properties of bulk high-entropy diborides for solar energy applications, J. Alloys Compd. 935 (2023) 167965, https://doi.org/10.1016/j.jallcom.2022.167965.
[50] ASTM E490-00a, Standard Solar Constant and Zero Air Mass Solar Spectral Irradiance Tables, ASTM International, West Conshohocken, PA, 2019, 2019.
[51] G.W.W. Wamelink, J.Y. Frissel, W.H.J. Krijnen, M.R. Verwoert, P.W. Goedhart, Can plants grow on Mars and the moon: a growth experiment on Mars and moon soil simulants, PLoS One 9 (2014) e103138, https://doi.org/10.1371/journal.pone.0103138.
[52] D.P. Glavin, C. Freissinet, K.E. Miller, et al., Evidence for perchlorates and the origin of chlorinated hydrocarbons detected by SAM at the Rocknest aeolian deposit in Gale Crater, J. Geophys. Res. Planets 118 (10) (2013) 1955–1973, https://doi.org/10.1002/jgre.20144.
[53] L.A. Leshin, P.R. Mahaffy, C.R. Webster, et al., Volatile, isotope, and organic analysis of martian fines with the Mars Curiosity rover, Science 341 (6153) (2013) 1238937, https://doi.org/10.1126/science.1238937.
[54] J.V. Clark, P.D. Archer, J.E. Gruener, D.W. Ming, V.M. Tu, P.B. Niles, S. A. Mertzman, JSC-Rocknest: a large-scale Mojave Mars Simulant (MMS) based soil simulant for in-situ resource utilization water-extraction studies, Icarus 351 (15) (2020) 113936, https://doi.org/10.1016/j.icarus.2020.113936.
[55] Y. Deng, F. Li, S. Zhou, X. Tao, Q. Zhou, Q. Feng, Integrated optimization of Martian regolith Sintering: tailoring microstructure and performance in a mineralogically replicated simulant, Acta Astronaut. 237 (2025) 224–235, https://doi.org/10.1016/j.actaastro.2025.08.038.
[56] M.A. Presley, R.A. Craddock, Thermal conductivity measurements of particulate materials: 3. Natural samples and mixtures of particle sizes, J. Geophys. Res. Planets 111 (2006) E9, https://doi.org/10.1029/2006JE002706.
[57] K. Seiferlin, P. Ehrenfreund, J. Garry, K. Gunderson, E. Hütter, G. Kargl, A. Maturilli, J.P. Merrison, Simulating Martian regolith in the laboratory, Planet. Space Sci. 56 (2008) 2009–2025, https://doi.org/10.1016/j.pss.2008.09.017.
[58] S. Nagihara, P. Ngo, M. Grott, Thermal properties of the mojave Mars regolith simulant in mars-like atmospheric conditions, Int. J. Thermophys. 43 (2022) 98, https://doi.org/10.1007/s10765-022-03023-y.
[59] M. Grott, T. Spohn, J. Knollenberg, C. Krause, T.L. Hudson, S. Piqueux, et al., Thermal conductivity of the Martian soil at the insight landing site from HP^3 active heating experiments, J. Geophys. Res. Planets 126 (2021), https://doi.org/10.1029/2021JE006861 e2021JE006861.
[60] J. Martikainen, O. Muñoz, T. Jardiel, J.C.G. Martín, M. Peiteado, Y. Willame, A. Penttilä, K. Muinonen, G. Wurm, T. Becker, Optical constants of Martian dust analogs at UV–visible–near-infrared wavelengths, Astrophys. J. Suppl. 268 (2) (2023) 47, https://doi.org/10.3847/1538-4365/acf0be.
[61] K.M. Cannon, D.T. Britt, T.M. Smith, R.F. Fritsche, D. Batcheldor, Mars global simulant MGS-1: a Rocknest-based open standard for basaltic martian regolith simulants, Icarus 317 (2019) 470–478, https://doi.org/10.1016/j.icarus.2018.08.019.
[62] J.F. Mustard, J.F. Bell, New composite reflectance spectra of Mars from 0.4 to 3.14 μm, Geophys. Res. Lett. 21 (1994) 353–356, https://doi.org/10.1029/94GL00198.
[63] C.C. Allen, R.V. Morris, D.J. Lindstrom, M.M. Lindstrom, J.P. Lockwood, JSC Mars-1: martian regolith simulant, in: Lunar and Planetary Institute Conference Abstracts, 1997, p. 29. https://www.lpi.usra.edu/meetings/LPSC98/pdf/1690.pdf. (Accessed 13 February 2026).
[64] Y. Deng, F. Li, S. Zhou, X. Tao, J. Liu, Z. Lin, Development of a mineralogically replicated Martian regolith simulant informed by Martian meteorites, Clean. Mater. 17 (2025) 100336, https://doi.org/10.1016/j.clema.2025.100336.
[65] E. Sani, L. Mercatelli, M. Meucci, A. Balbo, C. Musa, R. Licheri, R. Orrù, G. Cao, Optical properties of dense zirconium and tantalum diborides for solar thermal absorbers, Renew. Energy 91 (2016) 340–346, https://doi.org/10.1016/j.renene.2016.01.068.
[66] E. Sani, L. Mercatelli, M. Meucci, A. Balbo, L. Silvestroni, D. Sciti, Compositional dependence of optical properties of zirconium, hafnium and tantalum carbides for solar absorber applications, Sol. Energy 131 (2016) 199–207, https://doi.org/10.1016/j.solener.2016.02.045.
[67] E. Sani, D. Sciti, L. Silvestroni, A. Bellucci, S. Orlando, D.M. Trucchi, Tailoring optical properties of surfaces in wide spectral ranges by multi-scale femtosecond-laser texturing: a case-study for TaB_2 ceramics, Opt. Mater. 109 (2020) 110347, https://doi.org/10.1016/j.optmat.2020.110347.
[68] E. Sani, D. Sciti, S. Failla, A. Bellucci, M. Mastellone, S. Orlando, D.M. Trucchi, Bulk ceramics of lanthanum hexaboride with enhanced spectral selectivity and photothermal efficiency for novel hybrid thermal-thermionic solar absorbers, Sol. Energy 271 (2024) 112423, https://doi.org/10.1016/j.solener.2024.112423.
[69] E. Sani, D. Sciti, S. Failla, C. Melandri, A. Bellucci, S. Orlando, D.M. Trucchi, Multi-scale femtosecond-laser texturing for photothermal efficiency enhancement on solar absorbers based on TaB_2 ceramics, Nanomaterials 13 (10) (2023) 1692, https://doi.org/10.3390/nano13101692.
[70] J. Appelbaum, G.A. Landis, Photovoltaic arrays for Martian surface power, Acta Astronaut. 30 (1993) 127–142, https://doi.org/10.1016/0094-5765(93)90105-6.
[71] J. Appelbaum, D.J. Flood, Solar radiation on Mars, Sol. Energy 45 (6) (1990) 353–363, https://doi.org/10.1016/0038-092X(90)90156-7.
[72] M. Smith, D. Craig, N. Herrmann, et al., The artemis program: an overview of NASA's activities to return humans to the moon, in: 2020 IEEE Aerospace Conference, Big Sky, 2020, pp. 1–10, https://doi.org/10.1109/AERO47225.2020.9172323.
[73] M.T. Lemmon, M.J. Wolff, J.F. Bell III, M.D. Smith, B.A. Cantor, P.H. Smith, Dust aerosol, clouds, and the atmospheric optical depth record over 5 Mars years of the Mars Exploration Rover mission, Icarus 251 (2015) 96–111, https://doi.org/10.1016/j.icarus.2014.03.029.
[74] M.T. Lemmon, S.D. Guzewich, J.M. Battalio, M.C. Malin, Á. Vicente-Retortillo, M. P. Zorzano, J. Martín-Torres, R. Sullivan, J.N. Maki, M.D. Smith, J.F. Bell III, The Mars Science Laboratory record of optical depth measurements via solar imaging, Icarus 408 (2024) 115821, https://doi.org/10.1016/j.icarus.2023.115821.
[75] M.T. Lemmon, M.D. Smith, D. Viudez-Moreiras, M. de la Torre-Juarez, Á. Vicente-Retortillo, A. Munguira, A. Sanchez-Lavega, R. Hueso, G. Martinez, B. Chide, R. Sullivan, Dust, sand, and winds within an active Martian storm in Jezero crater, Geophys. Res. Lett. 49 (17) (2022), https://doi.org/10.1029/2022GL100126, 2022GL100126.
[76] Á. Vicente-Retortillo, F. Valero, L. Vázquez, G.M. Martínez, G.M., A model to calculate solar radiation fluxes on the Martian surface, J. Space Weather Space Clim. 5 (2015) A33, https://doi.org/10.1051/swsc/2015035.
[77] M. Alberghini, M. Morciano, L. Bergamasco, M. Fasano, L. Lavagna, G. Humbert, E. Sani, M. Pavese, E. Chiavazzo, P. Asinari, Coffee-based colloids for direct solar absorption, Sci. Rep. 9 (1) (2019) 4701, https://doi.org/10.1038/s41598-019-39032-5.